Monthly Notices of the ROYAL ASTRONOMICAL SOCIETY

MNRAS **527,** 10480–10506 (2024) https://doi.org/10.1093/mnras/stad3694
Advance Access publication 2023 December 4

Scanning for dark matter subhaloes in *Hubble Space Telescope* imaging of 54 strong lenses

James W. Nightingale [1,2]★ Qiuhan He [2] Xiaoyue Cao [3,4,5] Aristeidis Amvrosiadis [2] Amy Etherington,[1] Carlos S. Frenk [2] Richard G. Hayes,[1] Andrew Robertson [6] Shaun Cole [2] Samuel Lange,[2] Ran Li[3,4,5] and Richard Massey [1,2]

[1]*Department of Physics, Centre for Extragalactic Astronomy, Durham University, South Rd, Durham DH1 3LE, UK*
[2]*Department of Physics, Institute for Computational Cosmology, Durham University, South Rd, Durham DH1 3LE, UK*
[3]*National Astronomical Observatories, Chinese Academy of Sciences, 20A Datun Road, Chaoyang District, Beijing 100012, China*
[4]*School of Astronomy and Space Science, University of Chinese Academy of Sciences, Beijing 100049, China*
[5]*Institute for Frontiers in Astronomy and Astrophysics, Beijing Normal University, Beijing 102206, China*
[6]*Jet Propulsion Laboratory, California Institute of Technology, 4800 Oak Grove Drive, Pasadena, CA 91109, USA*

Accepted 2023 November 23. Received 2023 November 23; in original form 2023 September 20

ABSTRACT

The cold dark matter (DM) model predicts that every galaxy contains thousands of DM subhaloes; almost all other DM models include a physical process that smooths away the subhaloes. The subhaloes are invisible, but could be detected via strong gravitational lensing, if they lie on the line of sight to a multiply imaged background source, and perturb its apparent shape. We present a predominantly automated strong lens analysis framework, and scan for DM subhaloes in *Hubble Space Telescope* imaging of 54 strong lenses. We identify five DM subhalo candidates, including two especially compelling candidates (one previously known in SLACS0946 + 1006) where a subhalo is favoured after all of our tests for systematics. We find that the detectability of subhaloes depends upon the assumed parametric form for the lens galaxy's mass distribution, especially its degree of azimuthal freedom. Using separate components for DM and stellar mass reveals two DM subhalo candidates and removes four false positives compared to the single power-law mass model that is common in the literature. We identify 45 lenses *without* substructures, the number of which is key to statistical tests able to rule out models of, for example, warm or self-interacting DM. Our full analysis results are available at https://github.com/Jammy2211/autolens_subhalo.

Key words: gravitational lensing: strong – Galaxy: structure – dark matter.

1 INTRODUCTION

The nature by which cold dark matter (CDM) leads to the formation of the large-scale structure of the Universe, the 'cosmic web', has been modelled in incredible detail by state-of-the-art cosmological *N*-body simulations (Springel et al. 2005). The picture of hierarchical growth has been established, where density peaks of CDM within the Universe's initial density field collapse to form self-bound virialized haloes. The lowest mass haloes form first, and successively merge to form higher mass haloes, a process that occurs over the full range of halo masses in a self-similar manner. In conjunction with a cosmological constant, Λ, this process describes structure formation in our concordance cosmological model, lambda-CDM (ΛCDM), which on large scales has now made numerous testable predictions which have shown remarkable agreement with observations, such as the clustering of galaxies (Hildebrandt et al. 2017) and the growth of baryon acoustic oscillations (Anderson et al. 2014).

A key prediction of ΛCDM on smaller scales is the hierarchy of subhaloes within each dark matter (DM) halo (Diemand et al. 2008; Springel et al. 2008). This states that orbiting within every DM halo are many lower mass satellite haloes that it has previously accreted. This hierarchy extends on, with DM haloes hosting subhaloes that themselves host subhaloes (Diemand, Kuhlen & Madau 2007). CDM thus predicts an abundance of low-mass (10^{-3} to $10^{8}\,M_{\odot}$) haloes throughout the Universe. The majority of such haloes are completely dark, as radiation from the ultraviolet background reheats the intergalactic medium and prevents gas from cooling and forming stars (Sawala et al. 2016; Benitez-Llambay & Frenk 2020). Owing to this lack of luminous emission, DM haloes below masses of $10^{8.5}\,M_{\odot}$ are yet to be observed, with the lowest mass DM haloes known being those of Milky Way dwarf galaxies (Belokurov et al. 2014). Observing completely dark haloes below masses of $10^{8.5}\,M_{\odot}$ would provide evidence in favour of ΛCDM on scales smaller than previously tested. However, if one could definitively show their absence, it would indicate that a different model for the DM particle is needed, for example warmer flavours (Bode, Ostriker & Turok 2001). This would then disfavour a Weakly Interacting Massive Particle from being the DM, and would instead point to alternatives which change the relativistic properties of DM in the early universe, so as to suppress halo formation at low masses (e.g. the sterile neutrino, Shi & Fuller 1999).

Strong gravitational lensing, where a background source is multiply imaged by a foreground deflector galaxy, provides a means to

★ E-mail: james.w.nightingale@durham.ac.uk

detect DM subhaloes that do not emit light. When an extended source galaxy is lensed, light rays emanating from different regions of the source trace through (and are lensed by) different regions of the lens. The observed, distorted shape thus contains a high-resolution imprint of the distribution of mass in the lens. If a DM subhalo is along any line of sight, it will perturb the image in a unique and observable way. This technique has provided multiple detections of DM subhaloes (Vegetti et al. 2010, 2012, 2014; Hezaveh et al. 2016) as well as non-detections that further constrain the subhalo mass function (Ritondale et al. 2019b). These observations have been translated into constraints on sterile neutrino cosmologies (Vegetti et al. 2018; Enzi et al. 2021). The technique also recently led to the discovery of an ultramassive black hole (Nightingale et al. 2023b).

Much effort has gone into understanding which DM subhaloes this technique can detect. Sensitivity mapping has shown that *Hubble Space Telescope* (*HST*) imaging can detect subhaloes of mass $\sim 10^{9.0}\,M_{\odot}$, whereas higher resolution very long baseline interferometry probes masses as low as $\sim 10^{6.0}\,M_{\odot}$ (McKean et al. 2015; Li et al. 2016; Despali et al. 2018, 2022). These studies assume DM substructures lie on a mass–concentration relation (e.g. Ludlow et al. 2016). Instead, Amorisco et al. (2022) performed sensitivity mapping over the scatter in this relation and showed that DM haloes $\sim$0.5 dex lower in mass become detectable when they have a higher than average concentration. Furthermore, for DM cosmologies with a cut-off mass (e.g. around $\sim 10^{8.5}\,M_{\odot}$ for warmer DM with a sterile neutrino) high concentration haloes below this cut-off do not exist and therefore do not become detectable – amplifying the contrast between the expected number of detections in CDM and warmer models. DM substructures in the lens galaxy and line of sight objects at a different redshift to the lens are both detectable (Li et al. 2017; Despali et al. 2018, 2022; Amorisco et al. 2022; He et al. 2022), with their relative contributions depending on the redshifts of the lens and the source. If subhaloes within the lens galaxy are detected, then interpreting them in terms of DM models is subject to uncertainties due to galaxy formation, for example reductions in subhalo mass by tidal stripping or stellar feedback (Despali & Vegetti 2017). Line-of-sight objects are unaffected by this.

Subhalo analysis comprises two parts: (i) confirming that the inclusion of a parametric DM subhalo is favoured when fitting the lens data and; (ii) for the detection to be reproduced by a non-parametric model which adds corrections to the gravitational potential on top of the best-fitting mass model (Koopmans 2005; Vegetti & Koopmans 2009; Suyu et al. 2010; Ritondale et al. 2019b; Vernardos & Koopmans 2022). The latter, often called the 'potential corrections', requires that the non-parametric model of the convergence resembles a *local* over density of mass; the expected signal of a DM subhalo. However, the correction often produces non-zero convergence on larger *global* scales, due to systematics associated with the assumed mass model being too simple (e.g. Ritondale et al. 2019b). In this scenario, a DM subhalo candidate is rejected, irrespective of how much the parametric model favours the DM subhalo. Early implementations of the potential corrections relied on some level of human input to choose aspects like the regularization (Koopmans 2005; Vegetti & Koopmans 2009), whereas Vernardos & Koopmans (2022) recently placed the method in a Bayesian framework. This work does not use the potential corrections and therefore cannot make a definitive claim as to whether any subhalo detection is genuine or not. Our focus is to understand how different lens model assumptions impact whether a parametric DM subhalo is favoured.

This work presents a predominantly automated search for subhaloes in strong lenses using the open-source strong lens modelling software PYAUTOLENS[1] (Nightingale, Dye & Massey 2018; Nightingale et al. 2021b). The software approaches lens modelling using the same Bayesian framework as the methods of Vegetti & Koopmans (2009) and Hezaveh et al. (2016) but differs in many aspects of its implementation (e.g. the source reconstruction). We scan for subhaloes in a sample of 54 strong lenses from the Strong Lens Advanced Camera for Surveys (SLACS) survey (Bolton et al. 2008) and BOSS GALaxy-Lyα EmitteR sYstems (BELLS-GALLERY) sample (Shu et al. 2016). This sample includes 10 lenses analysed by Vegetti et al. (2010, 2014) and 16 of the systems analysed by Ritondale et al. (2019b). We therefore perform DM subhalo detection in 28 objects never previously analysed. Our results build on Etherington et al. (2022), who performed automated lens modelling with PYAUTOLENS in a sample of 59 strong lenses from the SLACS and BELLS-GALLERY samples and investigated the redshift evolution of the lens galaxy mass distributions (Etherington et al. 2023b).

After an initial analysis of the 54 strong lenses we focus on 'false positive' detections. Here, a lens model including a DM subhalo is favoured at $>3\sigma$ over a model without a DM subhalo, but more detailed investigation led us to conclude the result is spurious. This has been seen in previous studies and attributed to inflexibility of mass models to fit the complex distribution in real galaxies (Hsueh et al. 2016, 2017, 2018; He et al. 2023). To mitigate false positives, previous studies have employed strict criteria for a DM subhalo detection, for example requiring that the Bayesian evidence of the lens model with a DM subhalo is favoured at 5σ (Vegetti et al. 2014) or 10σ (Ritondale et al. 2019b). They are also flagged by the potential corrections technique discussed previously. Our results do not imply that any previous DM subhalo detections are false positives. Instead, we reproduce false positive signals found in previous studies (which are typically below the 5σ or 10σ threshold these studies used) and quantify which deficiencies in the strong lens model are the cause, in order to outline where improvements should be made in the future.

We place an emphasis on understanding what impact changing the lens galaxy mass model has on the final DM subhalo inference. We scan for DM subhaloes assuming a total of five different mass model parametrizations from the literature (Chu et al. 2013; Tessore & Metcalf 2015; Nightingale et al. 2019; O'Riordan, Warren & Mortlock 2020). We quantify whether fitting more complex models leads one to favour or reject a DM subhalo, when fitting a simpler model either did or did not. This is only possible because our analysis is predominantly automated, and therefore straightforward to repeat with a variety of model assumptions. Our large sample of 54 lenses yields the first quantitative study of how different types of model complexity impact subhalo detectability.

This paper is structured as follows. In Section 2, we describe the *HST* imaging data. In Section 3, we describe PYAUTOLENS and our substructure detection pipelines. In Section 4, we show results for fits to *HST* strong lenses. In Section 5, we discuss the implications of our measurements, and we give a summary in Section 6. In Appendix B, we show our substructure detection method works on simulated images. We assume a *Planck* 2015 cosmology throughout (Ade et al. 2016). The analysis scripts and data used in this work are publically available at https://github.com/Jammy2211/autolens_subhalo.

[1] https://github.com/Jammy2211/PyAutoLens

2 *HUBBLE SPACE TELESCOPE* DATA

In this work, we fit *HST* imaging of 54 strong lenses from the SLACS (Bolton et al. 2008) and BELLS-GALLERY (Shu et al. 2016) samples. Full details of these data sets and their data reduction are given in Bolton et al. (2008) and Shu et al. (2016). SLACS data are observed in the *HST* Advanced Camera for Surveys *F*814*W* band and BELLS-GALLERY the *HST* Wide Field Camera 3 *F*606*W* band. Etherington et al. (2022) describe post-processing steps which remove contaminating foreground light (e.g. of stars and line-of-sight galaxies) via a graphical user interface (GUI). We only use the gold sample presented in Etherington et al. (2022), which removes five lenses where a poor lens light subtraction would negatively impact the quality of the lens model.

3 METHOD

3.1 Overview

We perform lens modelling using the open-source software PYAUTOLENS, which is described in Nightingale & Dye (2015) and Nightingale et al. (2018, 2021b) and builds on the methods of Warren & Dye (2003, WD03 hereafter), Suyu et al. (2006), and Vegetti & Koopmans (2009). We compose pipelines which perform predominantly automated lens modelling using the probabilistic programming language PYAUTOFIT[2] (Nightingale, Hayes & Griffiths 2021a), a spin-off project of PYAUTOLENS which generalizes the methods used to model strong lenses into an accessible statistics library.

A concise visual overview of the PYAUTOLENS analysis performed in this work is shown in Fig. 1. Given an observed image of a strong lens the analysis: (i) defines a 3.5 arcmin circular mask within which the lens model is fitted (this mask extends beyond the lensed source in order to better constrain the lens light model); (ii) uses a model containing light and mass profiles for the lens to produce model images of the lens galaxy and lensed source, which are convolved with the instrumental point spread function (PSF) and compared to the data; (iii) reconstructs the source galaxy in the source plane using a Voronoi mesh and; (iv) produces a subhalo scanning map indicating how much a lens model with a DM subhalo at a specific location in the image plane increases the Bayesian evidence compared to a lens model without a DM subhalo.

We now describe each step in more detail. The following link (https://github.com/Jammy2211/autolens_likelihood_function) contains JUPYTER notebooks providing a visual step-by-step guide of the PYAUTOLENS likelihood function used in this work.

3.2 Light profiles

Light and mass profile quantities are computed using elliptical coordinates $\xi = \sqrt{x^2 + y^2/q^2}$, with minor to major axis-ratio q and position angle ϕ defined counterclockwise from the positive x-axis. For model fitting, these are parametrized as two components of ellipticity

$$\epsilon_1 = \frac{1-q}{1+q}\sin 2\phi, \;\; \epsilon_2 = \frac{1-q}{1+q}\cos 2\phi. \tag{1}$$

[2]https://github.com/rhayes777/PyAutoFit

Light profiles are modelled using one or more elliptical Sérsic profiles

$$I_{\rm Ser}(\xi) = I \exp\left\{-k\left[\left(\frac{\xi}{R}\right)^{\frac{1}{n}} - 1\right]\right\}, \tag{2}$$

which have up to seven free parameters: (x, y), the light centre in arcseconds, (ϵ_1, ϵ_2) the elliptical components, I, the intensity in electrons per second at the effective radius R in arcseconds and n, the Sérsic index. k is not a free parameter, but is instead a function of n (Ciotti & Bertin 1999). This study assumes a model with two Sérsic profiles which have the same centre, with each individual profile's intensities evaluated and summed. Parameters are given the superscripts 'bulge' and 'disc', which are used to distinguish which component of the lens galaxy they are modelling, for example, the Sérsic index of the bulge component is $n^{\rm bulge}$.

3.3 Mass profiles

3.3.1 Dark matter subhaloes

DM subhaloes (superscript 'sub') are modelled as a spherical Navarro–Frenk–White (NFW) profile. The NFW represents the universal density profile predicted for DM haloes by cosmological N-body simulations (Navarro, Frenk & White 1996, 1997; Zhao 1996), and with a volume mass density given by

$$\rho = \frac{\rho_{\rm s}^{\rm dark}}{(r/r_{\rm s}^{\rm dark})(1 + r/r_{\rm s}^{\rm dark})^2}. \tag{3}$$

The halo normalization is given by $\rho_{\rm s}^{\rm sub}$ and the scale radius in arcseconds by $r_{\rm s}^{\rm sub}$. The DM normalization is parametrized using $M_{200}^{\rm sub}$ (the enclosed mass in solar masses at the radius r_{200} within which the average density is 200 times the critical density of the Universe) as a free parameter. The scale radius is set via $M_{200}^{\rm sub}$ using the mean of the mass–concentration relation of Ludlow et al. (2016). The convergence is given by

$$\kappa(\xi) = 2\kappa^{\rm sub}\frac{1 - \mathcal{F}(\xi)}{\xi^2 - 1}, \tag{4}$$

where

$$\mathcal{F}(\xi) = \begin{cases} \frac{1}{\sqrt{\xi^2-1}}\arctan\sqrt{\xi^2-1} & : \xi > 1 \\ \frac{1}{\sqrt{1-\xi^2}}\operatorname{arctanh}\sqrt{1-\xi^2} & : \xi < 1 \\ 1 & : \xi = 1, \end{cases} \tag{5}$$

and $\kappa^{\rm sub}$ is related to the lens halo normalization by $\kappa^{\rm sub} = \rho_{\rm s} r_{\rm s}/\Sigma_{\rm cr}$ and $\Sigma_{\rm cr}$ is the critical surface density. The lens and source redshifts are used to perform unit conversions, for example, to calculate $M_{200}^{\rm sub}$ in solar masses. All DM subhaloes are assumed to be at the lens galaxy redshift.

3.3.2 Elliptical power law

For the lens mass model, we assume an elliptical power-law (PL) density profile representing the total mass of the lens (e.g. star and DM) of form

$$\kappa(\xi) = \frac{(3 - \gamma^{\rm mass})}{1 + q^{\rm mass}}\left(\frac{\theta_{\rm E}^{\rm mass}}{\xi}\right)^{\gamma^{\rm mass}-1}, \tag{6}$$

where parameters associated with the lens mass profile have superscript 'mass'. $\theta_{\rm E}^{\rm mass}$ is the model Einstein radius in arcseconds. The PL density slope is $\gamma^{\rm mass}$, and setting $\gamma^{\rm mass} = 2$ gives the singular isothermal ellipsoid (SIE) model. Deflection angles for the PL are

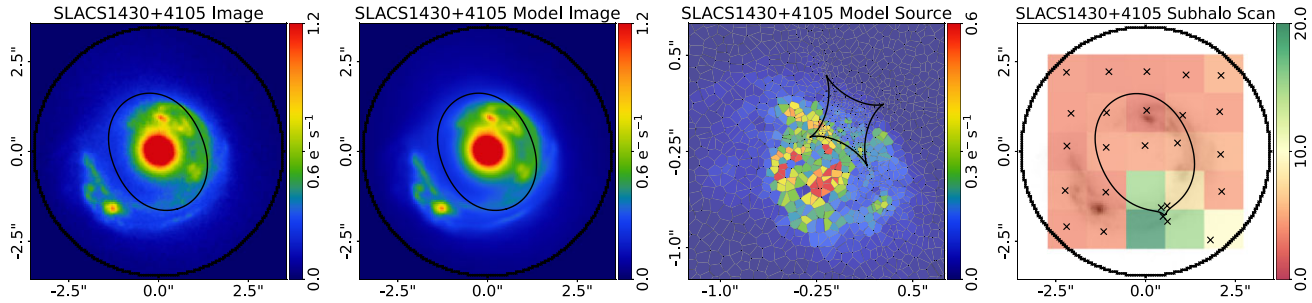

Figure 1. A concise visual overview of the PYAUTOLENS analysis performed in this study, shown for an example strong lens SLACS1430 + 4105. The images from left to right are: (i) the observed *HST* imaging data of SLACS1430 + 4105; (ii) the model lens light and lensed source inferred from a PYAUTOLENS model fit; (iii) the inferred model source in the source plane, which is reconstructed using a Voronoi mesh and; (iv) the subhalo scanning results, where the colour bar shows the log Bayesian evidence increase for lens models including a subhalo within 2D segments of the image plane. The solid lines show the tangential critical curves and caustics and crosses in the subhalo scanning results show the inferred subhalo $(x^{\rm sub},\ y^{\rm sub})$ coordinates for each model including a subhalo. The example subhalo scan of SLACS1430 + 4105 favours a DM subhalo at $(x^{\rm sub},\ y^{\rm sub}) \sim (0.2\,\text{arcsec}, -1.2\,\text{arcsec})$, however systematic tests of the lens mass model will reveal this is a false positive.

computed via an implementation of the method of Tessore & Metcalf (2015) in PYAUTOLENS.

3.3.3 *Broken power law*

We also fit the elliptical broken power-law (BPL) profile (O'Riordan, Warren & Mortlock 2019, 2020, 2021), again representing the total mass of the lens, with convergence

$$\kappa(r) = \begin{cases} \kappa_{\rm E}^{\rm mass} \left(r_{\rm b}^{\rm mass}/r\right)^{t_1^{\rm mass}}, & r \leq r_{\rm b}^{\rm mass} \\ \kappa_{\rm E}^{\rm mass} \left(r_{\rm b}^{\rm mass}/r\right)^{t_2^{\rm mass}}, & r > r_{\rm b}^{\rm mass} \end{cases}, \tag{7}$$

where $r_{\rm b}^{\rm mass}$ is the break radius in arcseconds, $\kappa_{\rm E}^{\rm mass}$ is the convergence at the break radius, $t_1^{\rm mass}$ is the inner slope, and $t_2^{\rm mass}$ is the outer slope.

3.3.4 *Power law with internal multipoles*

We fit an extension to the PL profile which includes multipole-like terms describing internal angular structure in its mass distribution, by extending the parametrization given by Chu et al. (2013). This model captures smooth deviations from ellipticity in the mass distribution. The functional form of the convergence is

$$\kappa(r, \phi) = \frac{1}{2}\left(\frac{\theta_{\rm E}^{\rm mass}}{r}\right)^{\gamma^{\rm mass}-1} k_m^{\rm mass} \cos(m(\phi - \phi_m^{\rm mass})), \tag{8}$$

where we express the convergence in polar coordinates, with r in arcseconds. m is the multipole order and $m = 4$. $k_m^{\rm mass}$ is the multipole strength and $\phi_m^{\rm mass}$ its orientation angle, which is defined counterclockwise from the positive x-axis. The multipole $\theta_{\rm E}^{\rm mass}$ and $\gamma^{\rm mass}$ values are fixed to that of the underlying PL. We parametrize $k_m^{\rm mass}$ and $\phi_m^{\rm mass}$ as multipole components $(\epsilon_1^{\rm mp},\ \epsilon_2^{\rm mp})$ which are given by

$$\phi_m^{\rm mass} = \arctan\frac{\epsilon_2^{\rm mp}}{\epsilon_1^{\rm mp}},\ k_m^{\rm mass} = \sqrt{\epsilon_1^{\rm mp2} + \epsilon_2^{\rm mp2}}. \tag{9}$$

3.3.5 *Stellar and dark matter mass*

We fit decomposed mass models for the lens, which decompose its mass into its stellar and dark components (in contrast to the PL models above). The stellar mass is modelled as a sum of Sérsic profiles which are tied to those of the light. The Sérsic profile given by equation () is used to give the light matter surface density profile

$$\kappa_{\rm Ser}(\xi) = \Psi\left[\frac{q\xi}{R}\right]^{\Gamma} I_{\rm Ser}(\xi), \tag{10}$$

where Ψ gives the mass-to-light ratio and Γ folds a radial dependence into the conversion of mass to light. A constant mass-to-light ratio is given for $\Gamma = 0$. This work assumes there are two light profile components (denoted the bulge and disc) which assume independent values of Ψ and Γ. We therefore do not assume that mass fully traces light. Deflection angles for this profile are computed via an adapted implementation of the method of Oguri (2021), which decomposes the convergence profile into multiple cored steep elliptical profiles and efficiently computes the deflection angles from each.

The DM component of the lens galaxy's host halo is given by an elliptical NFW profile, whose parameters have superscript 'dark'. This is again parametrized with $M_{200}^{\rm dark}$ as a free parameter and a scale radius set via the mean of the mass–concentration relation of Ludlow et al. (2016). The convergence is given by equation (5).

3.3.6 *Line-of-sight galaxies*

Nearby line-of-sight galaxies may be included as spherical isothermal spheres (SISs), corresponding to an SIE where $(\epsilon_1^{\rm mass},\ \epsilon_2^{\rm mass}) = (0, 0)$. To decide whether to include line-of-sight galaxies in the mass model we use a GUI, where a user looks at 10 arcsec cut-outs of each lens and clicks on up to two galaxies nearby to add to the mass model. Galaxies are selected subjectively based on their proximity and size. Each galaxy is then included as an SIS, the centre of which is fixed to the galaxy's brightest pixel and with a redshift that is the same as the lens galaxy. The prior on $\theta_{\rm E}^{\rm mass}$ for each SIS is a uniform prior from 0.0 to 0.5 arcsec. For the majority of line-of-sight galaxies a value of $\theta_{\rm E}^{\rm mass} = 0.5$ arcsec is significantly above the mass one would estimate based on its luminosity. This is an intentional choice not to use more informative priors, so that we can investigate how line-of-sight galaxies change the DM inference with maximal freedom.

Fig. 2 shows the five lenses with line-of-sight galaxies closest to the lens galaxy centre, which are all within 2.0 arcsec of it. These objects are close enough to the lensed source that we anticipate they will impact the inferred lens model. For the lenses SLACS0956 + 5100 and BELLS0918 + 5104 the line-of-sight galaxy is within the Einstein

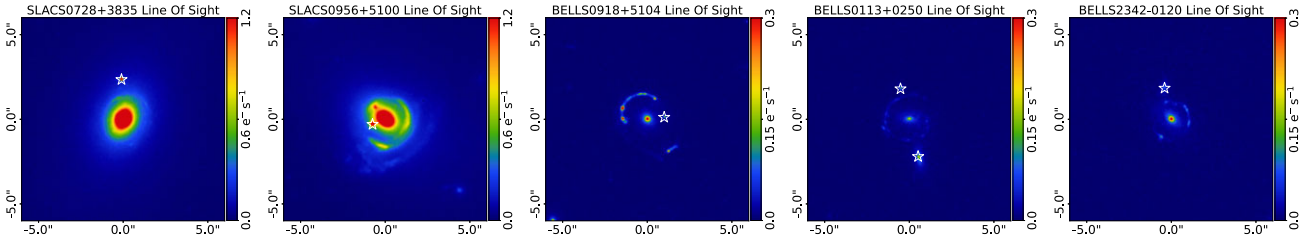

Figure 2. The five lenses with line-of-sight galaxies that are closest to the centre of their lens galaxy, which should have an impact on the inferred lens model. For two lenses, SLACS0956 + 5100 and BELLS0918 + 5104, the line-of-sight galaxy is within the Einstein radius, whereas for SLACS0728 + 3835, BELLS0113 + 0250, and BELLS2342-0120 the galaxy(s) are slightly outside the Einstein radius. Black stars mark the centre of each line-of-sight galaxy, which are modelled with SIS mass profiles fixed to these centres.

radius, whereas for SLACS0728 + 3835, BELLS0113 + 0250 and BELLS2342 − 0120 the galaxy(s) are slightly outside the Einstein radius. Models including line-of-sight galaxies for the remaining 49 lenses are performed, noting the galaxies are typically much further (e.g. over 4.0 arcsec) from the lens centre.

3.3.7 External shear

An external shear (superscript 'ext') field is included and parametrized as two elliptical components ($\gamma_1^{\rm ext}, \gamma_2^{\rm ext}$). The shear magnitude, $\gamma^{\rm ext}$, and orientation measured counterclockwise from north, $\phi^{\rm ext}$, are given by

$$\gamma^{\rm ext} = \sqrt{\gamma_1^{\rm ext^2} + \gamma_2^{\rm ext^2}}, \quad \tan 2\phi^{\rm ext} = \frac{\gamma_2^{\rm ext}}{\gamma_1^{\rm ext}}. \tag{11}$$

The deflection angles due to the external shear are computed analytically. Every mass model above is combined with an external shear. A recent study by Etherington et al. (2023a) suggests that this external shear component is representing missing complexity in the lens mass distribution, as opposed to line-of-sight galaxies.

3.4 Source model

After subtracting the foreground lens emission and ray-tracing coordinates to the source plane via the mass model, the source is reconstructed in the source plane using an adaptive mesh which accounts for irregular or asymmetric source morphologies. We use a Voronoi mesh with natural neighbour interpolation (Sibson 1981) and in Appendix B we compare DM subhalo results assuming different source reconstruction methods.

3.4.1 Mesh centres

The method first determines the centres of the I Voronoi source pixels. Initial fits overlay a rectangular Cartesian grid of shape ($y_{\rm pix}$, $x_{\rm pix}$) over the image plane, which extends to and from the mask edges (e.g. from −3.5 to 3.5 arcsec for the mask shown in Fig. 1). $y_{\rm pix}$ and $x_{\rm pix}$ are the height and width of this grid in pixels and are treated as free parameters. All coordinates on this uniform grid which fall within the mask are retained and traced to the source plane via the mass model (pixels outside the mask are discarded). These coordinates, M_i, are used as the centre of the Voronoi cells, which therefore trace the mass model magnification.[3]

[3]This corresponds to PYAUTOLENS's `VoronoiNNMagnification` mesh object.

Subsequent fits adapt the mesh centres M_i to the source's unlensed morphology. This uses a previous model of the lensed source emission, Ξ_j, which is used to compute the weights

$$W_j = \left(\frac{\Xi_j - \min \Xi}{\max \Xi_j - \min \Xi}\right) + W_{\rm floor} + \max \Xi_j. \tag{12}$$

The first term on the right-hand side runs from zero to one, where values closer to one correspond to the lensed source's brightest pixels. $W_{\rm floor}$ controls how much weight is given to the source's brightest pixels and is a free parameter in certain fits. W is passed to a weighted KMeans clustering algorithm (Pedregosa et al. 2011) to determine image-plane coordinates which are traced to the source plane. The KMeans assumes $N_{\rm pix}$ source pixels, which is treated as a free parameter in certain fits. This scheme adapts to the lensed source emission.[4]

3.4.2 Mapping matrix

The reconstruction computes the linear superposition of PSF-smeared source pixel images which best fits the observed image. This uses the mapping matrix f_{ij}, which maps the jth pixel of each lensed image to each source pixel i, giving a total of J lensed image pixels and I source pixels. When constructing f_{ij} we apply image-plane subgridding of degree 4 × 4, meaning that 16 × J subpixels are fractionally mapped to source pixels with a weighting of $\frac{1}{16}$, removing aliasing effects (Nightingale & Dye 2015).

Each image subpixel is mapped to multiple Voronoi source pixels weighted via interpolation. We use Voronoi natural neighbour interpolation via Sibson's (1981) technique. For every subpixel, j, the method considers a new polygon that adding this point to the Voronoi mesh computed from M_i would create. The new polygon captures some of the area that was previously covered by its neighbours, which the method computes and uses to compute the interpolation weights in f_{ij} as

$$w = f_{ij} = \frac{1}{\sum_{i=1}^{K} A_{\rm capture}} \sum_{k=1}^{K} A_{\rm capture}\, z_k, \tag{13}$$

where K is the number of neighbours of a given Voronoi cell i.[5]

[4]This corresponds to PYAUTOLENS's `VoronoiNNBrightnessImage` mesh objects.

[5]More details about the natural neighbour interpolation technique can be found at https://gwlucastrig.github.io/TinfourDocs/NaturalNeighborTinfourAlgorithm/index.html

3.4.3 Regularization

Performing an inversion using equation (13) by itself is ill-posed, therefore to avoid overfitting noise the solution is regularized using a linear regularization matrix $\mathbf{H}$ described by WD03. The matrix $\mathbf{H}$ applies a prior on the source reconstruction, penalizing solutions where the difference in reconstructed flux of neighbouring Voronoi source pixels is large. Initial fits use gradient regularization (see WD03) adapted to a Voronoi mesh (see Nightingale & Dye 2015).[6] DM subhalo results use a scheme which adapts the degree of smoothing to the reconstructed source's luminous emission and interpolates values at a cross of surrounding points.[7] The formalism for the calculation of these regularization matrices $\mathbf{H}$ is given in Appendix A.

3.4.4 Variance scaling

Lens galaxies can have complex morphologies which leave significant central residuals after subtraction via multiple Sérsic profiles, which the source reconstruction will attempt to fit. We mitigate this by allowing the method to increase the variances (the noise value in each image pixel) at the centre of an image. First, we estimate the fractional contribution in each pixel j from the lens light

$$\Omega_{\mathrm{Lens,j}} = \frac{Ł_{\mathrm{j}}}{T_{\mathrm{j}} + \omega_{\mathrm{Lens}}}, \tag{14}$$

where $Ł_{\mathrm{j}}$ and T_{j} are estimates of the lens light emission and total emission from a previous lens model and ω_{Lens} is a free parameter. Values of $Ł_{\mathrm{j}}$ or T_{j} less than 1 per cent their maximum value are rounded up to this value to ensure no values are negative. Ω_{Lens} is divided by its maximum value such that it ranges between values just above 0 and 1. Initial fits which do not have $Ł_{\mathrm{j}}$ and T_{j} vectors use σ_j^{obs}, the observed image statistical uncertainties. This contribution map is used to scale the noise in lens light dominated pixels as

$$\sigma_j = \omega_{\mathrm{Lens}} (\sigma_j^{\mathrm{obs}}\, \Omega_{\mathrm{Lens,j}})^{\omega_{\mathrm{Lens2}}}, \tag{15}$$

where ω_{Lens} and ω_{Lens2} are free parameters.

3.4.5 Inversion

Following the formalism of WD03, we define the data vector $\vec{D}_i = \sum_{j=1}^{J} f_{ij}(d_j - b_j)/(\sigma_j)^2$ and curvature matrix $F_{ik} = \sum_{j=1}^{J} f_{ij} f_{kj}/(\sigma_j)^2$, where d_j are the observed image flux values and b_j are the model lens light values. The source pixel surface brightnesses are given by $s = [F + H]^{-1}\vec{D}$ which are solved via a linear inversion that minimizes

$$\chi^2 + G_{\mathrm{L}} = \sum_{j=1}^{J} \left[\frac{(\sum_{\mathrm{i}=1}^{I} s_i f_{ij}) + b_j - d_j}{\sigma_j} \right]^2 + \boldsymbol{s}^T \mathbf{H} \boldsymbol{s}. \tag{16}$$

The term $\sum_{i=1}^{I} s_i f_{ij}$ maps the reconstructed source back to the image plane for comparison with the observed data and $G_{\mathrm{L}} = s^T H s$ is a regularization term.

The degree of smoothing is chosen objectively using the Bayesian formalism introduced by Suyu et al. (2006). The likelihood function is taken from Dye et al. (2008) and is given by

$$-2\ln \mathcal{Z} = \chi^2 + \boldsymbol{s}^T \mathbf{H} \boldsymbol{s} + \ln\,[\det(\mathbf{F} + \mathbf{H})] - \ln\,[\det(\mathbf{H})] + \sum_{j=1}^{J} \ln\left[2\pi(\sigma_j)^2\right]. \tag{17}$$

The step-by-step JUPYTER notebooks linked to in Section 3.1 describe how the different terms in this likelihood function compare and ranks different source reconstructions, allowing one to objectively determine the lens model that provides the best fit to the data in a Bayesian context.

3.5 Non-linear search

We use the nested sampling algorithm `dynesty` (Speagle 2020) to fit every lens model. We use the static sampler with random walk nested sampling, which tests revealed gave faster and more reliable lens model fits.

3.6 Lens modelling pipelines

The models of lens mass, lens light, and source light are complex and their parameter spaces are highly dimensional. Without human intervention or careful set up, the model-fitting algorithm (e.g. `dynesty`) may converge very slowly to the global maximum a posteriori solution or falsely converge on a local maximum. PYAUTOLENS therefore breaks the fit into a sequence of simpler fits. Using the probabilistic programming language PYAUTOFIT,[8] we fit a series of parametric lens models with growing complexity. Fits to simpler model parametrizations provide information which initializes subsequent fits to the next more complex model. We use the Source, Light, and Mass (SLaM) pipelines described by Etherington et al. (2022, hereafter E22), Cao et al. (2021), and He et al. (2023). Table 1 provides a step-by-step overview of the pipelines used in this work. The SLaM pipelines are available at https://github.com/Jammy2211/autolens_workspace.

An overview of the SLaM pipelines is as follows:

(i) *Source pipelines.* Initializes the Voronoi mesh source model by inferring a robust lens light subtraction (using a double Sérsic model) and total mass model (using an SIE plus shear). The initial stages of this pipeline fit the source using a parametric Sérsic profile and perform the variance scaling described in Section 3.4.4.

(ii) *Light pipeline.* Uses fixed values of the mass and source parameters corresponding to the maximum-likelihood model of the Source pipeline. This is the first time the lens light is fitted for simultaneously with a Voronoi mesh source instead of Sérsic profile. The lens mass is therefore again described by an SIE plus shear. The only free parameters in this pipeline are those of a double Sérsic lens light model and ω_{Lens} which controls the magnitude of variance scaling. The maximum-likelihood lens light subtracted image inferred by this pipeline is output for use by additional fits investigating lens modelling systematics.

(iii) *Mass pipeline:* Fits a PL, BPL, PL with multipoles, decomposed mass model or PL with line-of-sight galaxies, which are all more complex than the SIE fitted previously. The lens light is fixed to the maximum-likelihood model of the Light pipeline.

(iv) *Subhalo pipeline.* Determines the increase in log Bayesian evidence when a DM subhalo is included in the lens model, which is described next in Section 3.7.

[6] This corresponds to the PYAUTOLENS regularization scheme `Constant`.
[7] This corresponds to the PYAUTOLENS regularization scheme `AdaptiveBrightnessSplit`.
[8] https://github.com/rhayes777/PyAutoFit

Table 1. Composition of the SLaM pipelines that make up our uniform analysis. The name of each pipeline phase is given in the second column in bold text. This is an adaptation and extension of the table presented by Etherington et al. (2022), who used the SLaM pipelines to fit *HST* imaging of strong lenses. After the phases **SI**[4], **LP**[1], and **MT**[1] the best-fitting model images (the Ξ_j and Ł_j) are updated for the adaptive mesh, regularization, and variance scaling features. Their associated parameters are refit via a standalone dynesty fit using a fixed lens model.

Pipeline	Phase	Galaxy component	Model	Varied	Prior info	Phase description
Source parametric	**SP**[1]	Lens light	Sérsic + Exp	✓	–	Fit only the lens light model and subtract it from the data image.
	SP[2]	Lens mass	SIE + shear	✓	–	Fit mass model and source light using lens subtracted image from **SP**[1].
		Source light	Sérsic	✓	–	
	SP[3]	Lens light	Sérsic + Exp	✓	–	Refit the lens light model with default priors and fit the mass and source models with priors informed from **SP**[2].
		Lens mass	SIE + shear	✓	**SP**[2]	
		Source light	Sérsic	✓	**SP**[2]	
Source inversion	**SI**[1]	Lens light	Sérsic + Exp	✓	**SP**[3]	Fix lens light and mass parameters from **SP**[3] and fit magnification adaptive Voronoi mesh and constant regularization parameters.
		Lens mass	SIE + shear	✓	**SP**[3]	
		Source light	Voronoi magnification	✓	–	
	SI[2]	Lens light	Sérsic + Exp	✗	**SP**[3]	Refine the lens mass model parameters, keeping lens light and source parameters fixed to those from previous phases.
		Lens mass	SIE + shear	✗	**SP**[3]	
		Source light	Voronoi magnification	✓	**SI**[1]	
	SI[3]	Lens light	Sérsic + Exp	✓	**SP**[3]	Fit brightness adaptive Voronoi mesh and luminosity adaptive regularization. Lens parameters fixed from **SP**[3].
		Lens mass	SIE + shear	✓	**SP**[3]	
		Source light	Voronoi brightness	✗	–	
	SI[4]	Lens light	Sérsic + Exp	✗	**SP**[3]	Refine lens mass model parameters using Voronoi Brightness grid. Fix lens light and source parameters to previous phases.
		Lens mass	SIE + shear	✗	**SI**[2]	
		Source light	Voronoi brightness	✓	**SI**[3]	
Light parametric	**LP**[1]	Lens light	Sérsic + Sérsic	✓	✓	Fit lens light parameters with broad uniform priors. Lens mass and source parameters fixed from **SI**[4].
		Lens mass	SIE + shear	✗	**SI**[4]	
		Source light	Voronoi brightness	✗	**SI**[4]	
Mass total	**MT**[1]	Lens light	Sérsic + Sérsic	✗	**LP**[1]	Fit the lens mass parameters, with subset of priors informed from **SI**[4]. Lens and source light are fixed from **LP**[1] and **SI**[4].
		Lens mass	See Section 4.7	✓	**SI**[4]	
		Source light	Voronoi brightness	✗	**LP**[1]	
Subhalo	**SH**[1]	Lens light	Sérsic + Sérsic	✗	**LP**[1]	Fit the lens mass parameters, with priors informed from **MT**[1]. Lens and source light are fixed from **LP**[1] and **SI**[4].
		Lens mass	See Section 4.7	✓	**MT**[1]	
		Source light	Voronoi brightness	✗	**MT**[1]	
	SH[2]	Lens light	Sérsic + Sérsic	✗	**LP**[1]	Performs grid search of DM subhhaloes (see Section 3.7).
		Lens mass	See Section 4.7 + subhalo	✓	**MT**[1]	
		Source light	Voronoi brightness	✗	**MT**[1]	
	SH[3]	Lens light	Sérsic + Sérsic	✗	**LP**[1]	Fits for DM subhalo using priors based on **SH**[2]. Bayesian evidence compared to **SH**[1] for DM subhalo inference.
		Lens mass	See Section 4.7 + subhalo	✓	**MT**[1]	
		Source light	Voronoi brightness	✗	**MT**[1]	

The SLaM pipelines use prior passing (see E22) to initialize the regions of parameter space that `dynesty` will search in later `dynesty` fits, based on the results of earlier fits. The priors of every lens model fitted in this work can be found at https://github.com/Jammy2211/autolens_subhalo. Priors are set up carefully to ensure they are sufficiently broad to not omit viable lens model solutions.

3.7 Subhalo scanning

Including a subhalo in the mass model produces a complex and multimodal parameter space that a nested sampler like `dynesty` may struggle to sample efficiently and robustly. We tested a model-fitting approach which simply adds a subhalo to a lens model assuming broad uniform priors on the subhalo's image-plane position ($x^{\rm sub}$, $y^{\rm sub}$) and mass $M_{200}^{\rm sub}$. However, these fits did not always reliably infer the subhalo's input properties on simulated data sets.

We instead perform a grid search of `dynesty` searches, where each grid-search cell places uniform priors on the image plane ($x^{\rm sub}$, $y^{\rm sub}$) position of the subhalo, spatially confining it to a small 2D square segment of the image plane. We perform 25 model fits (corresponding to a 5×5 grid in the image plane), where the size of the box containing this grid is chosen via visual inspection of each lens. An example subhalo scan is shown in Fig. 1. This removes the multimodality in the parameter space created by the subhalo model, simplifying it such that the global maxima solution in parameter space is reliably inferred. For each grid cell, log uniform priors with masses between 10^6–$10^{12}\,{\rm M}_\odot$ are assumed for $M_{200}^{\rm sub}$. We always assume the subhalo is at the same redshift as the lens galaxy (e.g. single plane lensing).

Once a grid search is complete, a final non-linear search is performed which provides accurate constraints on the subhalo mass $M_{200}^{\rm sub}$ and image-plane coordinates ($x^{\rm sub}$, $y^{\rm sub}$). The subhalo centre's priors are set via prior passing, using the highest evidence model of the grid search (the lens model parameters also use this result). This prior allows for a wider range of subhalo centres than the uniform priors defining each 2D grid cell, but is centred on the highest evidence grid search model, ensuring `dynesty` sampling remains reliable. The subhalo retains its log uniform prior on $M_{200}^{\rm sub}$ with masses between 10^6–$10^{12}\,{\rm M}_\odot$, to avoid overly tight priors reducing the inferred error. `dynesty` settings are adjusted to sample parameter space more thoroughly at the expense of longer computational run-time.

We quantify whether models including a subhalo are favoured using the Bayesian evidence, $\mathcal{Z}$, of the lens models with and without a DM subhalo. The evidence is the integral of the likelihood over the prior and therefore naturally includes a penalty term for including too much complexity in a model. $\mathcal{Z}$ is inferred by `dynesty` (see equation of Speagle 2020) and therefore available for every fit performed in this work. We define the log evidence difference in favour of the lens model with a DM subhalo as

$$\Delta \ln \mathcal{Z} = \ln \mathcal{Z}_{\rm sub} - \ln \mathcal{Z}_{\rm none}, \tag{18}$$

where $\ln \mathcal{Z}_{\rm sub}$ is the Bayesian evidence inferred by the fit after the subhalo scanning grid search and $\ln \mathcal{Z}_{\rm none}$ is the evidence of the lens model without a subhalo before the grid search. Superscripts are added to $\Delta \ln \mathcal{Z}$ to denote model fits which make different assumptions, for example, $\Delta \ln \mathcal{Z}^{\rm Base}$ denotes the increase in log evidence for the baseline lens model with a subhalo assuming a PL mass model, double Sérsic lens light model and where the source is reconstructed on a Voronoi mesh. An increase of $\Delta \ln \mathcal{Z} = 4.5$ for one model over another corresponds to odds of 90:1 in favour of that model; a 3σ preference. An increase of $\Delta \ln \mathcal{Z} = 12.5$ corresponds to a 5σ preference. Our criteria for a candidate subhalo detection is that we infer $\Delta \ln \mathcal{Z} > 10$. The subhalo scanning analysis is the same as that used in He et al. (2023), who modelled strong lenses simulated via cosmological simulations with PYAUTOLENS.

4 RESULTS

We now present the results of subhalo scanning different data sets. In Section 4.1, we give a concise summary of fits to simulated lens data sets which are described fully in Appendix B. We use these results as a starting point to investigate false positives DM subhalo detections due to lens modelling systematics.

4.1 Subhalo scanning on simulated data

In Appendix B, we simulate and fit a sample of 16 strong lenses, in four groups of lenses with the same lens and source galaxies but with DM subhaloes of masses $10^{10.5}$, $10^{10.0}$, $10^{9.5}{\rm M}_\odot$ or no subhalo. The simulated lenses are idealized, because their lens light (double Sérsic) and mass (PL plus shear) are simulated using the same model assumed to fit the data. Cautioning that these conclusions only hold in this idealized scenario, a summary is as follows:

(i) For 7 out of the 8 data sets containing a $10^{10.5}$ or $10^{10.0}\,{\rm M}_\odot$ DM subhalo the analysis successfully detects the DM subhalo.

(ii) For 2 out of the 4 data sets containing a $10^{9.5}\,{\rm M}_\odot$ DM subhalo the analysis successfully detects the input DM subhalo. For the two data sets where the input DM subhalo is not detected we attribute this to the data not being sensitive enough.

(iii) For all four data sets not containing a DM subhalo, we correctly disfavour a DM subhalo provided the source reconstruction has sufficiently high resolution.

(iv) Our subhalo inference does not depend on the source reconstruction assumptions (e.g. it is insensitive to using a different regularization scheme).

(v) The lens mass model is degenerate with the DM subhalo, whereby the inferred mass model changes its inferred parameters to 'absorb' some of the DM subhalo signal.

False positive DM subhalo detections were not seen for the mock lenses (provided the source reconstruction was high enough resolution). This procedure therefore verifies that for our analysis of *HST* imaging of real lenses, false positives are because the lens model assumptions are not robust (or it is a geniune DM subhalo detection).

4.2 Subhalo scanning on *HST* data with simple models

We now present subhalo scanning of *HST* imaging of 54 strong lenses from the SLACS (Bolton et al. 2008) and BELLS-GALLERY (Shu et al. 2016) samples. Results for each sample are given separately, because the compact nature of BELLS-GALLERY sources changes their sensitivity to DM subhaloes (Despali et al. 2022). We first present results for our simplest baseline lens model, which assumes two Sérsic profiles with the same centres for the lens light, a PL plus external shear mass model and Voronoi mesh source reconstruction. All fits adopt a 3.5 arcsec circular mask.

Column 2 of Table 2 lists $\Delta \ln \mathcal{Z}^{\rm Base}$, the log evidence increase for a model including a subhalo for the 37 SLACS lenses. 14 out of 37 lenses favour the inclusion of a DM subhalo and meet our criterion of $\Delta \ln \mathcal{Z}^{\rm Base} > 10$. Fig. 3 shows the corresponding subhalo grid search results for these objects, where from the top left rightwards and then downwards lenses are plotted in descending order of $\Delta \ln \mathcal{Z}^{\rm Base}$. The lens SLACS2341 + 0000 infers the highest value, $\Delta \ln \mathcal{Z}^{\rm Base} = 157.51$. 24 lenses are non-detections with $\Delta \ln \mathcal{Z}^{\rm Base} < 10$. Column 3 of Table 2 shows the inferred subhalo masses $M_{200}^{\rm sub}\,{\rm M}_\odot$, which span $10^{8.39}$ and $10^{11.98}\,{\rm M}_\odot$ for models where $\Delta \ln \mathcal{Z}^{\rm Base} > 10$.

Table 2. The log Bayesian evidence increase $\Delta \ln \mathcal{Z}$ of subhalo scanning for the SLACS sample.

Lens name	$\Delta \ln \mathcal{Z}^{\rm Base}$	$\log_{10}[M_{200}^{\rm sub}/{\rm M}_\odot]$	$\Delta \ln \mathcal{Z}^{\rm Light}$	Light $\Delta \ln \mathcal{Z}$decrease?	$\Delta \ln \mathcal{Z}^{\rm Source}$	Source $\Delta \ln \mathcal{Z}$decrease?	$\Delta \ln \mathcal{Z}^{\rm BPL}$	$\Delta \ln \mathcal{Z}^{\rm Multipole}$	$\Delta \ln \mathcal{Z}^{\rm Decomp}$	Mass $\Delta \ln \mathcal{Z}$ decrease?	$\Delta \ln \mathcal{Z}^{\rm Los}$	Los $\Delta \ln \mathcal{Z}$decrease?	$\Delta \ln \mathcal{Z}^{\rm Final}$	Category
SLACS2341 + 0000	**157.51**	$11.98^{+0.02}_{-0.21}$	**32.7**	✓	**24.91**	✗	**25.94**	**18.46**	8.52	✓	Demag	✗	**11.61**	ND/Los
SLACS1432 + 6317	**79.34**	$11.96^{+0.04}_{-0.30}$	8.65	✓	−0.23	✗	Demag	**10.87***	1.83	✗	**15.24***	✗	1.82	ND
SLACS0946 + 1006	**52.86**	$11.91^{+0.09}_{-0.55}$	**75.76***	✗	**72.36**	✗	**74.27**	**76.81**	**22.52**	✓	**29.24**	✓	**22.51**	Cand
SLACS0956 + 5100	**40.11**	$11.77^{+0.23}_{-0.58}$	**18.04**	✓	**23.35**	✗	**12.07**	**11.52**	**10.78**	✓	**31.37**	✗	**10.77**	ND/Los
SLACS1020 + 1122	**38.71**	$11.93^{+0.07}_{-0.43}$	5.36	✓	2.1	✗	3.23	0.99	7.81	✗	4.42	✗	0.99	ND
SLACS1250 + 0523	**30.87**	$10.68^{+0.84}_{-0.33}$	8.23	✓	**13.41**	✗	**18.68**	−2.09	**17.4**	✓	8.17	✗	3.16	ND/FP-PL
SLACS1032 + 5322	**27.79**	$11.96^{+0.04}_{-0.28}$	−0.49	✓	0.81	✗	Demag	−1.68	6.26	✗	−0.08	✗	2.82	ND
SLACS0959 + 0410	**21.39**	$11.91^{+0.09}_{-0.43}$	**49.66***	✗	**19.62**	✓	Demag	5.95	**28.12**	✗	3.37	✓	−24.90	ND/FP-PL
SLACS0029-0055	**20.58**	$11.12^{+0.50}_{-0.52}$	**33.92***	✗	4.82	✓	**18.75***	7.22	**35.15***	✗	1.36	✗	**21.69**	Cand/Decomp
SLACS1023 + 4230	**19.73**	$11.14^{+0.44}_{-0.60}$	4.32	✓	4.82	✗	1.26	−1.31	0.72	✗	1.5	✗	−1.30	ND
SLACS1143-0144	**19.17**	$11.94^{+0.06}_{-0.50}$	5.35	✓	2.37	✗	0.65	−0.45	**17.23***	✗	**13.29***	✗	−0.44	ND
SLACS0157-0056	**16.38**	$11.52^{+0.48}_{-5.40}$	**17.65**	✗	−0.57	✓	−0.29	−0.93	1.06	✗	−0.37	✗	−0.57	ND
SLACS1451-0239	**13.78**	$8.39^{+2.45}_{-2.36}$	−1.09	✓	−0.44	✗	−0.67	2.43	2.98	✗	−0.22	✗	−0.22	ND
SLACS1430 + 4105	**12.0**	$10.80^{+0.50}_{-0.69}$	**11.14**	✗	**13.4**	✗	5.25	**14.06**	6.54	✗	**15.72**	✗	6.53	ND/FP-PL
SLACS0903 + 4116	9.72	$11.89^{+0.11}_{-0.76}$	**15.35**	✗	3.91	✓	3.79	1.05	9.13	✗	2.16	✗	3.90	ND
SLACS2303 + 1422	9.66	$11.10^{+0.47}_{-0.79}$	1.1	✗	2.14	✗	2.82	−1.6	1.73	✗	8.06	✗	3.80	ND
SLACS1213 + 6708	8.73	$11.88^{+0.12}_{-1.10}$	1.1	✗	3.49	✗	0.21	0.25	1.52	✗	1.18	✗	1.52	ND
SLACS1630 + 4520	8.45	$10.89^{+0.45}_{-0.64}$	5.41	✗	−0.58	✗	−0.43	Demag	−1.66	✗	7.15	✗	−1.66	ND
SLACS0822 + 2652	7.94	$11.87^{+0.13}_{-0.92}$	2.67	✗	−1.25	✗	2.1	1.46	2.19	✗	−1.92	✗	−1.38	ND
SLACS1029 + 0420	4.03	$11.75^{+0.25}_{-3.47}$	−1.28	✗	2.17	✗	Demag	3.71	**22.57***	✗	1.71	✗	**10.57**	Cand/Decomp
SLACS2300 + 0022	4.49	$9.41^{+2.57}_{-3.40}$	−1.7	✗	−0.46	✗	−0.29	−0.47	2.23	✗	1.47	✗	−0.46	ND
SLACS1205 + 4910	4.12	$6.92^{+1.42}_{-0.91}$	8.97	✗	2.14	✗	0.63	2.25	**31.15***	✗	−2.38	✗	1.87	ND
SLACS0912 + 0029	3.92	$11.89^{+0.11}_{-1.05}$	3.1	✗	1.19	✗	2.36	1.49	5.33	✗	0.33	✗	2.07	ND
SLACS1402 + 6321	3.41	$9.74^{+1.36}_{-3.73}$	−0.14	✗	−0.53	✗	−2.01	−1.03	4.64	✗	−0.7	✗	0.01	ND
SLACS0252 + 0039	3.32	$10.71^{+0.69}_{-1.76}$	−1.04	✗	6.53	✗	−0.89	**17.66***	5.26	✗	5.89	✗	−0.89	ND
SLACS1218 + 0830	3.25	$11.06^{+0.92}_{-5.04}$	−0.12	✗	0.24	✗	−1.35	0.16	2.42	✗	−0.92	✗	0.23	ND
SLACS1525 + 3327	3.15	$10.94^{+1.02}_{-4.81}$	1.34	✗	0.24	✗	Demag	Demag	Demag	✗	Demag	✗	0.24	ND
SLACS1627-0053	2.52	$11.37^{+0.58}_{-5.12}$	2.51	✗	7.9	✗	3.25	8.18	5.27	✗	5.93	✗	7.89	ND
SLACS0008-0004	2.51	$8.83^{+2.94}_{-2.82}$	1.59	✗	−1.44	✗	−1.43	−0.38	−0.46	✗	−0.28	✗	−1.43	ND
SLACS1420 + 6019	1.92	$10.81^{+1.06}_{-1.96}$	0.64	✗	3.11	✗	0.6	−1.56	2.79	✗	2.94	✗	2.79	ND
SLACS0330-0020	1.19	$10.83^{+0.36}_{-4.66}$	−1.44	✗	−0.88	✗	2.29	**11.04***	8.12	✗	3.69	✗	0.01	ND
SLACS1142 + 1001	0.71	$11.41^{+0.59}_{-5.17}$	−0.42	✗	0.31	✗	0.78	0.53	**10.47***	✗	0.64	✗	6.00	ND
SLACS0936 + 0913	0.33	$10.30^{+1.56}_{-4.26}$	−2.2	✗	−1.12	✗	−0.8	−2.01	0.25	✗	0.33	✗	−1.12	ND
SLACS2238-0754	−3.36	$8.72^{+2.91}_{-2.70}$	−0.1	✗	0.78	✗	−2.39	**17.66***	8.53	✗	0.62	✗	−0.22	ND
SLACS0216-0813	−1.43	$11.31^{+0.68}_{-5.23}$	−3.4	✗	−0.65	✗	0.55	−1.41	−0.12	✗	−1.04	✗	−0.11	ND
SLACS0737 + 3216	−1.34	$9.43^{+2.51}_{-3.38}$	1.21	✗	0.33	✗	−1.99	−0.74	0.99	✗	−0.52	✗	0.99	ND
SLACS0728 + 3835	−4.17	$8.71^{+0.28}_{-0.27}$	−6.58	✗	2.92	✗	Demag	**16.18***	1.81	✗	−10.47	✓	0.25	ND/FP-Los

Notes. Column 1 gives the lens name. Column 2 shows $\Delta \ln \mathcal{Z}^{\rm Base}$ for the baseline model, which assumes a PL plus shear lens mass model, a two Sérsic lens light subtraction, and a Voronoi mesh source reconstruction. Column 3 gives the corresponding inferred DM subhalo mass at 3σ confidence intervals. Columns 4–13 show the results of different systematic tests. Column 4 shows $\Delta \ln \mathcal{Z}^{\rm Light}$ values, where lens light cleaned data are fitted (see Section 4.3). Column 5 indicates if $\Delta \ln \mathcal{Z}^{\rm Base} - \Delta \ln \mathcal{Z}^{\rm Light} > 10$ (*e.g. does improving the lens light subtraction decrease* $\Delta \ln \mathcal{Z}$?). Column 6 shows $\Delta \ln \mathcal{Z}^{\rm Source}$ values, where source only masked data are fitted (see Section 4.4). Column 7 indicates if $\Delta \ln \mathcal{Z}^{\rm Light} - \Delta \ln \mathcal{Z}^{\rm Source} > 10$ (*e.g. does improving the source reconstruction decrease* $\Delta \ln \mathcal{Z}$?). Columns 8–10 show fits assuming different mass models: a BPL ($\Delta \ln \mathcal{L}^{\rm BPL}$), a PL with internal multipoles ($\Delta \ln \mathcal{L}^{\rm Multipole}$) and a decomposed mass model ($\Delta \ln \mathcal{L}^{\rm Decomp}$). Column 11 indicates whether $\Delta \ln \mathcal{Z}^{\rm Source} - \max(\Delta \ln \mathcal{Z}^{\rm BPL}, \Delta \ln \mathcal{Z}^{\rm Multipole}, \Delta \ln \mathcal{Z}^{\rm Decomp}) > 10$ (*e.g. does assuming any of the three more complex mass models decrease* $\Delta \ln \mathcal{Z}$?). Column 12 shows $\Delta \ln \mathcal{L}^{\rm Los}$ values, which fit a PL plus shear mass model that includes line-of-sight galaxies. Column 13 indicates if $\Delta \ln \mathcal{Z}^{\rm Source} - \Delta \ln \mathcal{Z}^{\rm Los} > 10$ (*e.g. does including line-of-sight galaxies decrease* $\Delta \ln \mathcal{Z}$?). Bold text indicates any fit above the detection threshold of $\Delta \ln \mathcal{Z} = 10.0$. Asterisks symbols indicate that $\Delta \ln \mathcal{Z}$ increases by over 10 for any of the four comparisons shown in the table (*e.g. does improving the lens light, source, mass model or including line-of-sight galaxies increase* $\Delta \ln \mathcal{Z}$?). Column 13 shows $\Delta \ln \mathcal{Z}^{\rm Final}$, the highest evidence of any mass model with a DM subhalo (corresponding to fits given in columns 5, 7, 8, 9, 11) minus the highest evidence of any mass model without a DM subhalo. The final column categorizes each DM subhalo result: *ND* for non-detection, Cand for candidate, FP-PL for power-law mass false positive, and FP-Los for line-of-sight false positive. Entries labelled 'Demag' are solutions where the fit inferred an unphysical solution (see Section 4.7).

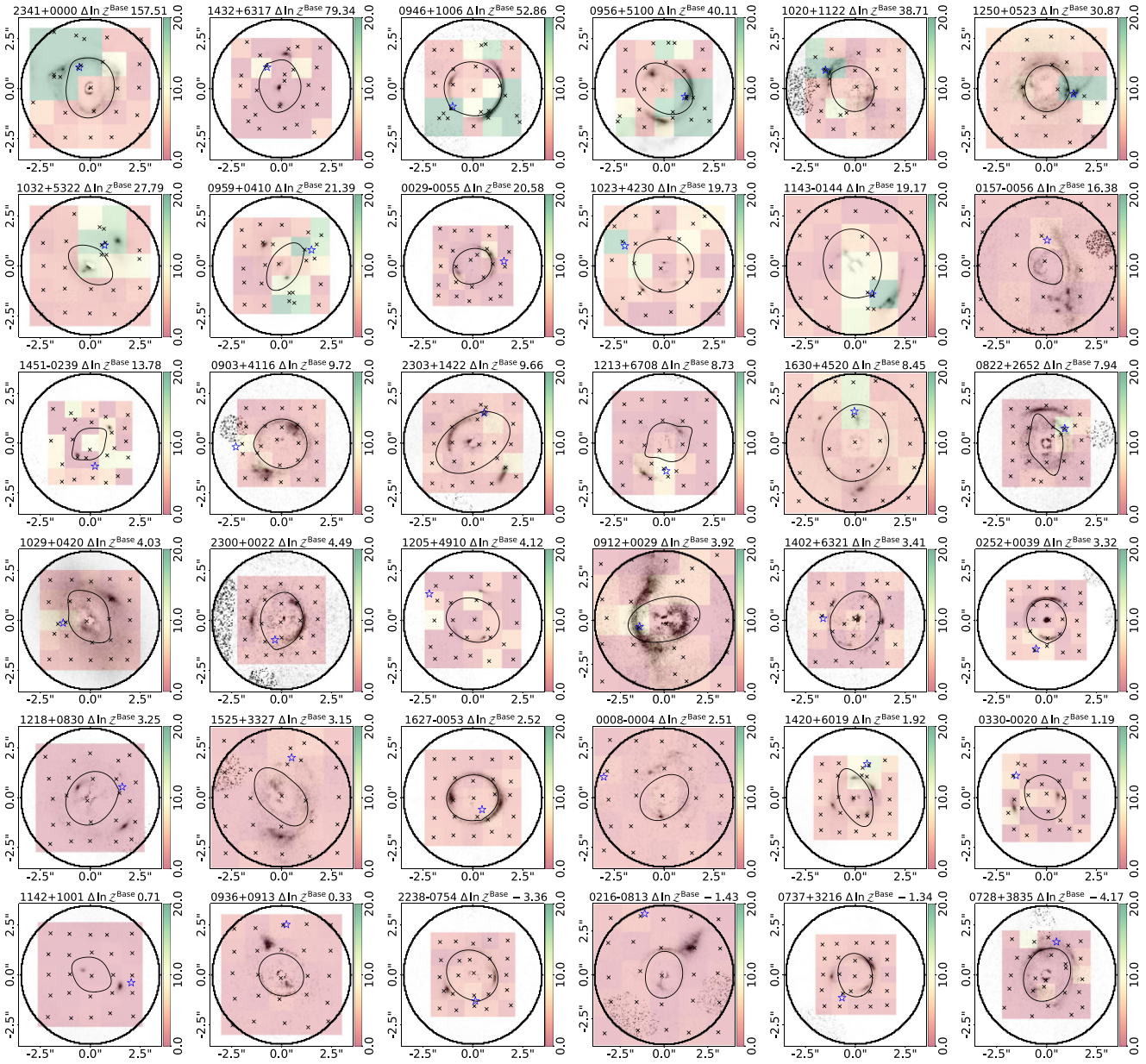

Figure 3. The subhalo scanning results of all SLACS lenses. Each scan uses a 5 × 5 grid of `dynesty` searches fitting a PL plus shear model with a subhalo whose (x, y) coordinates are confined to a 2D grid cell via uniform priors (see Section 3.7). Fits are shown in descending order of highest log evidence increase. The background images show the lens subtracted data, where the lens subtraction uses a double Sérsic fit. In Section 4, we demonstrate that the majority of these DM subhalo candidates are false positives. The coloured grid shows the increase of log evidences of each subhalo scan grid cell. The $\Delta \ln \mathcal{Z}^{\rm Base}$ values in each plot title correspond to the **SH3** fit performed after the subhalo grid search where the subhalo position priors extend beyond a small 2D cell. This $\Delta \ln \mathcal{Z}^{\rm Base}$ value is sometimes much higher than the inferred grid search values and is why certain lenses show predominantly low log evidence increases but have high overall $\Delta \ln \mathcal{Z}^{\rm Base}$ values in the title (e.g. SLACS1432 + 6316). The star shows the DM subhalo's maximum a posteriori inferred location for this fit. The colour bar ranges between 0 and 20 so that candidate DM subhaloes ($\Delta \ln \mathcal{Z}^{\rm Base} > 10$ are coloured distinctly from non-candidates). Certain lenses (e.g. SLACS1020 + 1122 on its left-hand side) show patches of noise, which are a result of emission from a foreground galaxy or star being removed via the noise-scaling GUI described in Etherington et al. (2022). The lens SLACS1430 + 4105, shown in Fig. 1, is omitted from this figure.

Column 2 of Table 3 lists $\Delta \ln \mathcal{Z}^{\rm Base}$ for all 16 BELLS-GALLERY lenses and Fig. 4 shows the corresponding subhalo scanning results. 7 out of 16 lenses meet our criterion of producing $\Delta \ln \mathcal{Z}^{\rm Base} > 10$. Four lenses give $\Delta \ln \mathcal{Z}^{\rm Base} > 100$. Nine lenses are non-detections with $\Delta \ln \mathcal{Z}^{\rm Base} < 10$. Table 3 also shows the inferred subhalo masses $M_{200}^{\rm sub}$, which again span $10^{8.3}$ and $10^{11.98}$ $M_\odot$ for models where $\Delta \ln \mathcal{Z}^{\rm Base} > 10$.

4.3 Subhalo scanning with different lens light subtraction

To investigate whether an inaccurate lens light subtraction produces false positives we fit lens light cleaned data sets. These are produced using a GUI which replaces the observed flux counts in the image data with Gaussian noise and increases the variances in all image pixels which – from visual inspection – appear to predominately contain lens light subtraction residuals. The pixels therefore do

Table 3. As Table 2, but for the BELLS-GALLERY sample instead of SLACS.

Lens name	$\Delta \ln \mathcal{Z}^{\rm Base}$	$\log_{10}[M_{200}^{\rm sub}/{\rm M}_\odot]$	$\Delta \ln \mathcal{Z}^{\rm Light}$	Light $\Delta \ln \mathcal{Z}$ decrease?	$\Delta \ln \mathcal{Z}^{\rm Source}$	Source $\Delta \ln \mathcal{Z}$ decrease?	$\Delta \ln \mathcal{Z}^{\rm BPL}$	$\Delta \ln \mathcal{Z}^{\rm Multipole}$	$\Delta \ln \mathcal{Z}^{\rm Decomp}$	Mass $\Delta \ln \mathcal{Z}$ decrease?	$\Delta \ln \mathcal{Z}^{\rm Los}$	Los $\Delta \ln \mathcal{Z}$ decrease?	$\Delta \ln \mathcal{Z}^{\rm Final}$	Category
BELLS0755 + 3445	**1287.01**	$11.98^{+0.02}_{-0.10}$	**1360.14***	✗	**1268.78**	✓	**1155.44**	**860.44**	**889.39**	✓	**184.49**	✓	1155.43	X
BELLS0918 + 5104	**520.91**	$9.31^{+0.01}_{-0.01}$	**323.52**	✓	**417.56***	✗	**250.44**	**248.04**	**193.93**	✓	**247.81**	✓	248.04	X
BELLS0029 + 2544	**278.85**	$10.99^{+0.12}_{-0.04}$	−164.99	✓	**157.26***	✗	−1269.31	**10.78**	−35.81	✓	−37.86	✓	24.74	X
BELLS0201 + 3228	−13.76	$8.30^{+0.01}_{-0.01}$	−3.1*	✗	−62.65	✓	−52.48*	**38.39***	1.37*	✗	−44.7*	✗	−52.47	X
BELLS1226 + 5457	**151.34**	$11.95^{+0.05}_{-0.24}$	**96.47**	✓	**105.9**	✗	**97.29**	**72.0**	**97.33**	✓	**22.46**	✓	**79.08**	Cand
BELLS1116 + 0915	**110.36**	$6.68^{+1.19}_{-0.66}$	1.6	✓	−0.36	✗	None	1.32	0.9	✗	−1.47	✗	−0.35	ND
BELLS1110 + 2808	**11.14**	$11.82^{+0.17}_{-3.90}$	4.37	✗	3.71	✗	0.32	1.03	3.98	✗	−0.19	✗	0.32	ND
BELLS0742 + 3341	9.29	$10.39^{+0.04}_{-0.19}$	7.59	✗	−3.59	✓	−2.58	−1.83	1.42	✗	−1.03	✗	−3.58	ND
BELLS1110 + 3649	6.0	$9.77^{+0.43}_{-0.55}$	**21.3***	✗	**12.65**	✗	**20.26**	**14.99**	3.05	✗	**10.82**	✗	3.04	ND/FP-PL
BELLS0237 − 0641	5.64	$6.91^{+2.20}_{-0.38}$	−8.41	✓	−0.96	✗	0.75	3.74	2.1	✗	2.1	✗	−0.95	ND
BELLS0856 + 2010	5.41	$7.85^{+2.33}_{-1.08}$	9.14	✗	−1.77	✓	Demag	−0.11	1.57	✗	−0.09	✗	1.53	ND
BELLS1201 + 4743	1.25	$8.65^{0.96}_{-1.23}$	3.11	✗	**20.36***	✗	**16.52**	3.59	3.69	✓	**25.58**	✗	**18.11**	Cand
BELLS2228 + 1205	0.02	$10.27^{+0.27}_{-0.05}$	1.46	✗	2.23	✗	−2.0	−1.4	2.38	✗	−2.0	✗	2.22	ND
BELLS0113 + 0250	−1.41	$10.71^{+0.60}_{-0.05}$	**29.99***	✗	8.55	✓	**11.37**	−7.81	−1.0	✓	−0.17	✗	8.55	ND
BELLS2342 − 0120	−7.09	$8.20^{+2.59}_{-0.48}$	**17.97***	✗	**16.61**	✗	**13.19**	5.62	**23.69**	✓	2.81	✓	**13.18**	ND/FP-Los
BELLS1141 + 2216	−18.2	$9.41^{+0.19}_{-0.32}$	−2.13*	✗	3.86	✗	0.73	2.64	3.88	✗	**10.08**	✗	0.72	ND

not contribute to the likelihood function given by equation (17). An example is shown in Fig. 5. The log evidence increases by including a DM subhalo for fits using the lens light cleaned data set is defined as $\Delta \ln \mathcal{Z}^{\rm Light}$, which is compared to $\Delta \ln \mathcal{Z}^{\rm Base}$ to isolate the dependence on the lens light subtraction.

The second and fourth columns of Table 2 show $\Delta \ln \mathcal{Z}^{\rm Base}$ and $\Delta \ln \mathcal{Z}^{\rm Light}$ values for SLACS, where for nine lenses (ticks in column five) fitting the lens light cleaned data decreases $\Delta \ln \mathcal{Z}$ by more than 10 ($\Delta \ln \mathcal{Z}^{\rm Base} - \Delta \ln \mathcal{Z}^{\rm Light} > 10$). This includes seven lenses which switch from candidate DM subhaloes to non-detections, because $\Delta \ln \mathcal{Z}^{\rm Light} < 10$ and $\Delta \ln \mathcal{Z}^{\rm Base} > 10$. Table 3 shows the same values for BELLS-GALLERY, where for 5 lenses $\Delta \ln \mathcal{Z}$ decreases by more than 10 and two lenses switch from favouring a DM subhalo to not. There are also three BELLS-GALLERY lenses where $\Delta \ln \mathcal{Z}^{\rm Light} > 10$ and $\Delta \ln \mathcal{Z}^{\rm Base} < 10$, meaning that fitting the lens light cleaned data means a DM subhalo is favoured when it was not for the baseline model.

Fig. 6 shows the observed image (left column), lens subtracted image (left-centre column), normalized residuals (right-centre column), and source reconstructions (right column) of SLACS2341 + 0000, for fits to the original data (top row) and lens light cleaned data (bottom row). This is the SLACS lens with the largest decrease of $\Delta \ln \mathcal{Z}^{\rm Light}$ compared to $\Delta \ln \mathcal{Z}^{\rm Base}$. There is evidence that the lens galaxy has undergone a recent merger, with the residuals showing tidal stream features to the left, above and right of the lensed source. The lens light subtraction also shows a central dipole feature indicating the galaxy has not yet dynamically settled post-merger. The source reconstruction shown in the top right panel reconstructs these lens light features towards the left, top, and right of the source plane. The bottom right panel shows these are not present in the source reconstruction of the lens light cleaned data, because the lens light residuals have been removed. The incorrect reconstruction of lens light features is responsible for the large decrease in $\Delta \ln \mathcal{Z}^{\rm Light}$.

Visual inspection of other lenses which show a large reduction in $\Delta \ln \mathcal{Z}$ when fitting lens light cleaned data indicates similar residuals are often present, which are therefore responsible for a DM subhalo being incorrectly favoured. However, they are typically not post-merger features like in SLACS2341 + 0000 but fainter lens galaxy morphological features like a central bulge or bar.

There will also be a more a subtle interplay between the lens subtraction and leftover lensed source emission, which to some degree will impact the DM subhalo inference. However, this is not responsible for the large changes of $\Delta \ln \mathcal{Z} > 10$ considered here. We note also that variance scaling (see Section 3.4.4) was intended to mitigate these false positives, but is clearly insufficient in many lenses.

By removing lens light residuals via a GUI, this source of DM subhalo false positives is successfully mitigated against. All remaining systematic tests therefore fit data which has been treated in this way.

4.4 Subhalo scanning with different source resolution

To investigate whether insufficient resolution of the source reconstruction leads to false positives we perform fits using source-only masks. These masks retain only image pixels with significant lensed source emission, an example of which is shown in Fig. 5. A GUI is used to mask the specific regions of the data which contain lensed source emission. All pixels outside of this custom mask are not ray-traced to the source plane and therefore are not used to construct the Voronoi mesh and reconstruct the source. This is in contrast to the lens light cleaned data above, which retained the 3.5 arcsec

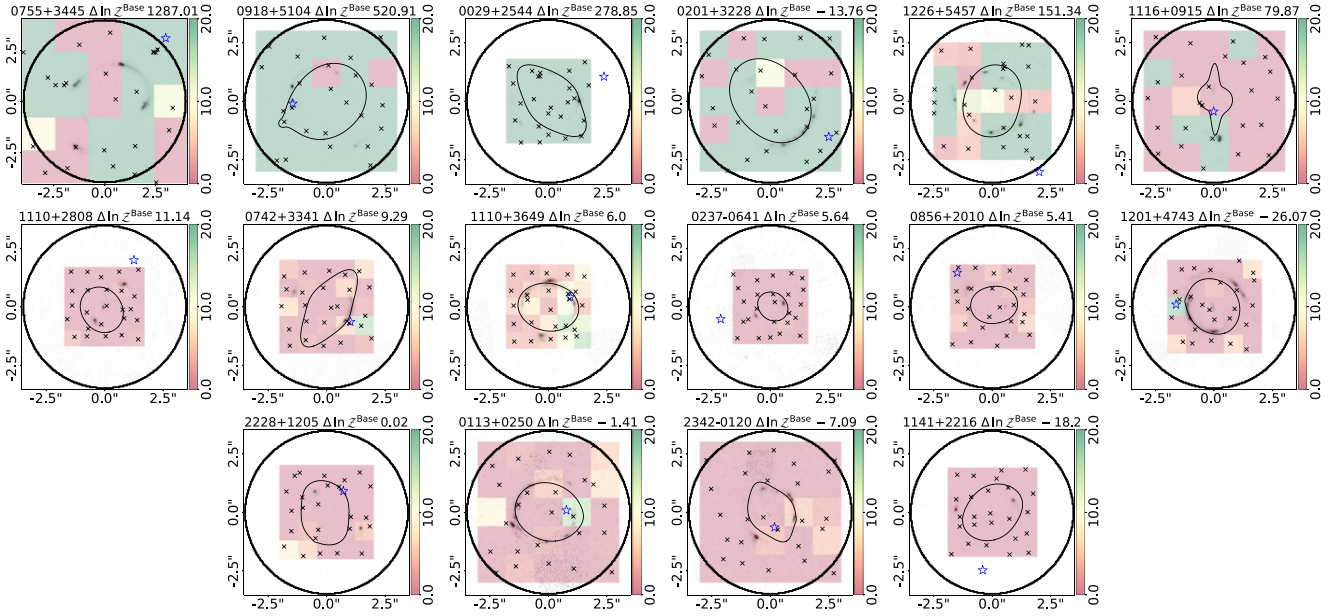

Figure 4. As Fig. 3, but for the BELLS-GALLERY sample instead of SLACS.

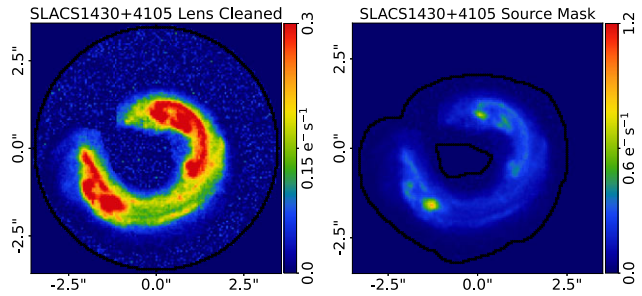

Figure 5. Illustration of the data augmentation schemes used to test for different systematics in the DM subhalo analysis, using the example lens SLACS1430 + 4105 (the image with the default 3.5 arcsec mask is shown in Fig. 1). The left panel illustrates lens light cleaned data, where image regions containing predominantly signal from the lens light have their signal replaced with Gaussian noise, and their corresponding variances increased to arbitrarily large values (meaning the pixels do not contribute to the likelihood). These image pixels are still ray traced to the source plane and reconstructed by the Voronoi mesh. Lens light cleaned data isolates whether lens light residuals are a systematic on the subhalo results (by comparing to fits using the default masks) and it uses evidence increases denoted $\Delta \ln \mathcal{Z}^{\rm Light}$. The right panel illustrates a source-only mask where the removed image pixels are not ray-traced to the source plane at all. The source reconstruction therefore dedicates more Voronoi cells to image pixels containing predominately the lensed source. Source-only masks isolate whether insufficient source resolution impacts the subhalo result (by comparing to fits using lens light-cleaned data) and evidence increases are denoted $\Delta \ln \mathcal{Z}^{\rm Source}$.

circular mask. The pixels outside the custom mask therefore also do not contribute to the χ^2 given in equation (17). A Voronoi mesh using a source-only mask therefore dedicates a larger fraction of Voronoi cells to reconstructing the source's brighter central regions. The number of source pixels is also fixed to 2500, the upper limit of the prior for previous fits using a circular mask. The log evidence increase by including a DM subhalo for fits using a source-only mask is defined as $\Delta \ln \mathcal{Z}^{\rm Source}$, which is compared to $\Delta \ln \mathcal{Z}^{\rm Light}$ to isolate the dependence on the source resolution.

The fourth and sixth columns of Table 2 show the $\Delta \ln \mathcal{Z}^{\rm Light}$ and $\Delta \ln \mathcal{Z}^{\rm Source}$ values for SLACS. For four lenses (ticks in column 7) a higher resolution source model decreases $\Delta \ln \mathcal{Z}$ by more than 10 ($\Delta \ln \mathcal{Z}^{\rm Light} - \Delta \ln \mathcal{Z}^{\rm Source} > 10$). This includes three lenses which go from candidate DM subhaloes to non-detections ($\Delta \ln \mathcal{Z}^{\rm Light} > 10$ and $\Delta \ln \mathcal{Z}^{\rm Source} < 10$). Table 3 shows the same values for BELLS-GALLERY, where for five lenses $\Delta \ln \mathcal{Z}$ decreases by more than 10 and none switch from DM subhalo candidates to non detections. The lens BELLS1201 + 4743, marked with an asterix in column 6 of Table 3, switches from a DM non-detection ($\Delta \ln \mathcal{Z}^{\rm Light} < 10$) to a candidate DM subhalo ($\Delta \ln \mathcal{Z}^{\rm Source} > 10$).

Fig. 7 shows the lens subtracted images and source reconstructions of SLACS0903 + 4116, a lens where $\Delta \ln \mathcal{Z}^{\rm Light} = 18.54$ and $\Delta \ln \mathcal{Z}^{\rm Source} = 3.83$. The higher resolution source reconstruction produced using the source-only mask reconstructs more structure, improving the overall lens analysis such that a DM subhalo is no longer favoured.

The DM subhalo results therefore depend on the source resolution. All remaining systematic tests therefore use source-only masks.

4.5 Catastrophic failures

Before considering results for different mass models, we highlight four lenses where no mass model produces a satisfactory fit: BELLS0755 + 3445, BELLS0918 + 5104, BELLS0029 + 2544, and BELLS0201 + 3228. Fig. 8 shows the four lenses, where the residuals exceed 6σ in a large fraction of image-pixels containing the lensed source's emission. For the remaining 50 out of 54 lenses in our sample, the residuals of the lensed source are within $\sim 3\sigma$. These four lenses are catastrophic failures – the significant residuals indicate that none of the lens models fitted in this work can attain a good quality of fit. We assign them to the category X for catastrophic failure and discard them from subsequent sections (noting that a DM subhalo is favoured in three of these lenses). Ritondale et al. (2019b) discuss BELLS0755 + 3445 as a lens where their fit produced significant residuals.

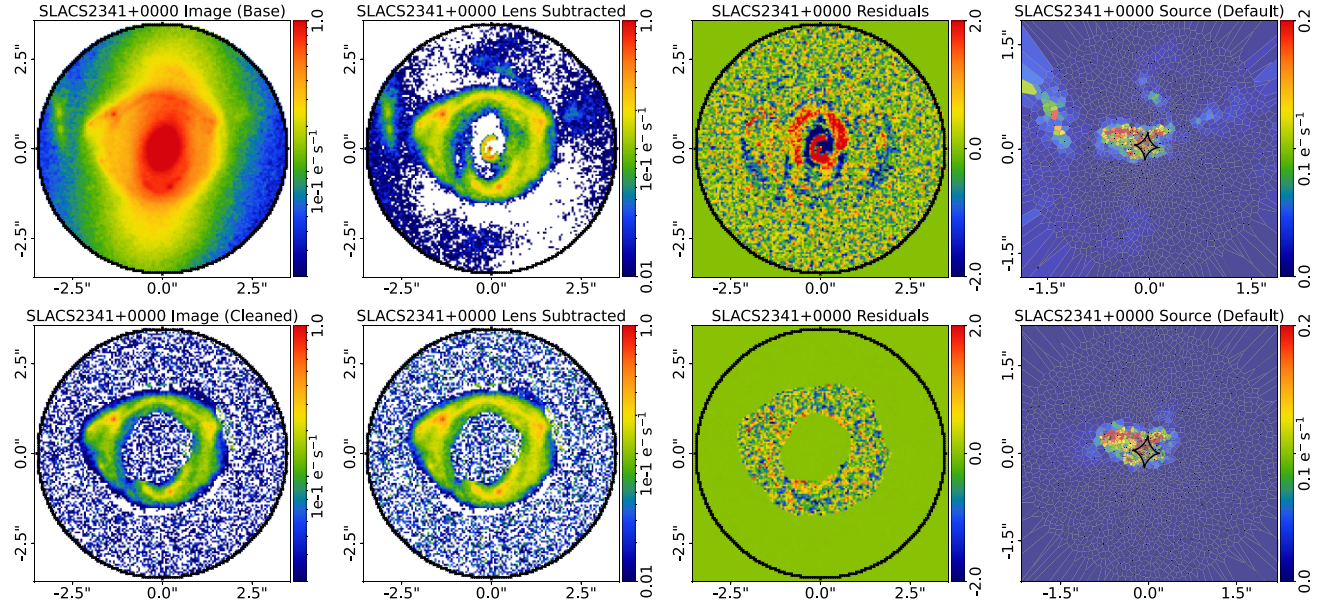

Figure 6. How removing lens light subtraction residuals (by fitting lens light cleaned data) can remove DM subhalo candidates, illustrated using SLACS2341 + 0000. The images (from left to right) are the observed image, lens subtracted image, normalized residuals (after subtracting the lens and lensed source models from the data), and source reconstruction. The top row shows fits to the original data and bottom row the lens light cleaned data. For SLACS2341 + 0000, the top row shows that the double Sérsic lens light subtraction leaves significant residuals in the centre and to the east, north, and west of the image, because of non-symmetric emission indicative of a post-merger. The source reconstruction (right panel) fits these lens light residuals, as it cannot distinguish lens and source emission. This is why a DM subhalo is incorrectly favoured. The lens light cleaned data removes these lens light residuals, such that the source reconstruction only reconstructs the source. The evidence for a DM subhalo in turn reduces significantly. In other lenses where a DM subhalo candidate is removed by fitting the lens light cleaned data, similar residuals are seen if a double Sérsic lens light model is used to subtract the lens light, but to a lesser degree. These are typically not due to post-merger features like in SLACS2341 + 0000, but other irregular morphological features (e.g a central bulge or disc-like structure).

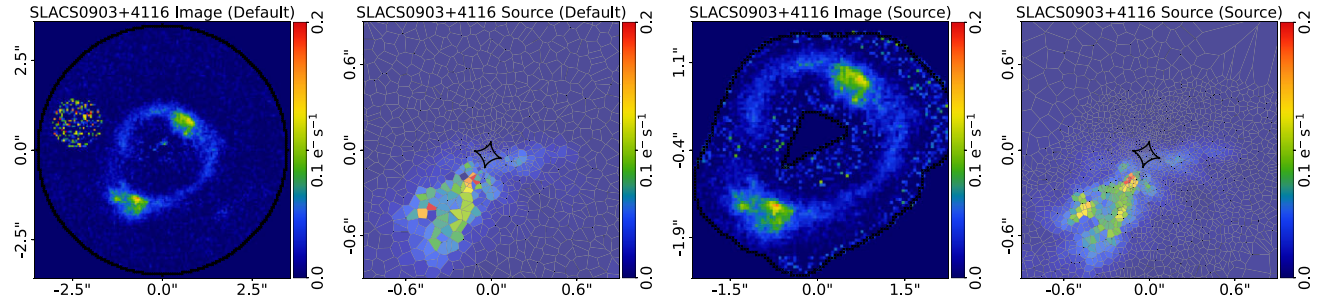

Figure 7. How making the source reconstruction higher resolution (by using a source-only mask) may remove a DM subhalo candidate, using the lens SLACS0903 + 4116. For this lens, the default 3.5 arcsec mask gives $\Delta \ln \mathcal{Z}^{\rm Light} = 15.35$, whereas the source-only mask gives $\Delta \ln \mathcal{Z}^{\rm SO} = 3.91$. Fits using the default 3.5 arcsec mask (left panels) and source-only mask (right panels) are shown, showing the lens subtracted image and Voronoi source mesh. Using a source only mask reconstructs the source using more Voronoi pixels, resolving source structure such that the lens model no longer favours a DM subhalo.

4.6 Overall subhalo scanning results

Using source-only masks, we compare the DM subhalo inferences after fitting all five different mass models: the PL, BPL, PL with multipoles, decomposed mass model, and PL with line-of-sight galaxies. Before comparing how different mass models change the DM subhalo inference, we first consider $\Delta \ln \mathcal{Z}^{\rm Final}$, which is the the highest $\ln \mathcal{Z}$ value inferred assuming any of the five mass models with a DM subhalo minus the highest $\ln \mathcal{Z}$ value inferred for any mass model without a DM subhalo. $\Delta \ln \mathcal{Z}^{\rm Final}$ is given in the second last column of Tables 2 and 3.

There are eight lenses which meet our criteria $\Delta \ln \mathcal{Z}^{\rm Final} > 10$. However, we assign three of these lenses as non-detections, because they have line-of-sight galaxies or post-merger features visible in their residuals, suggesting the model favouring a DM subhalo is likely spurious. These lenses have the category tag 'ND/Los' for non-detection due to line-of-sight in the final column of Tables 2 and 3. We are therefore left with five DM subhalo candidates, which are assigned the category 'Cand' for candidate and a total of 45 non-detections, which are assigned the category 'ND'.

A small subset of model fits do not produce a physically plausible lens model, instead inferring the demagnified solutions described by Maresca, Dye & Li (2021). Their $\Delta \ln \mathcal{Z}$ values are omitted from the results and their corresponding results table entries have the entry 'Demag'. This occurred for 11 fits in total: 8 out of 54 fits for the

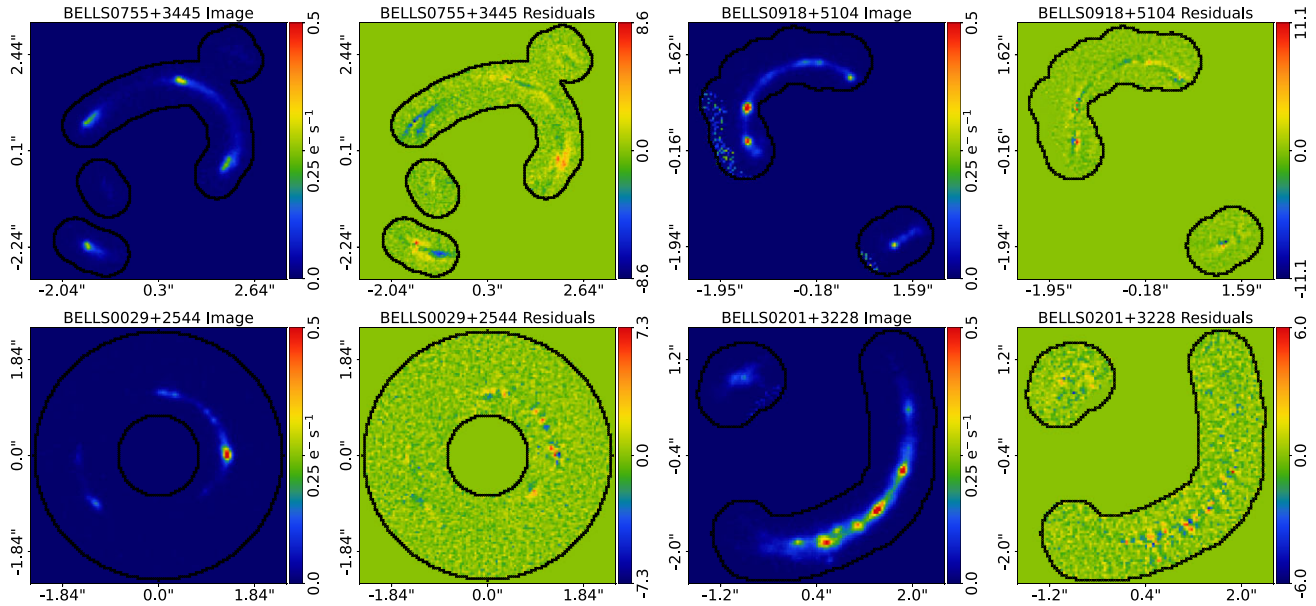

Figure 8. The four lenses which are catastrophic failures, based on their residuals exceeding of 3σ outliers across many image pixels in two or more lensed source images. The lensed subtracted images and normalized residuals of each lens are shown (a normalized residual value indicates how much of a σ outlier the fit is).

Table 4. In four lenses, the PL mass model favoured a DM subhalo but at least one of the three more complex mass models (BPL, PL with multipoles, decomposed mass model) did not. This table shows the inferred $\Delta \ln \mathcal{Z}$ values for the complex mass model minus $\Delta \ln \mathcal{Z}$ inferred for the simpler PL (both models without a subhalo). The values are inferred in the **SH**[1] stage of the SLaM pipeline. Values of $\Delta \ln \mathcal{Z} > 10$ indicate that the more complex mass model is favoured over the PL, which occurs for all four lenses.

Lens name	BPL	PL with multipoles	Decomposed
SLACS1250 + 0523		31.84	
SLACS0959 + 0410		44.52	
SLACS1430 + 4105	4.56		15.69
BELLS1110 + 3649			11.81

BPL, 2 out of 54 fits for the PL with multipoles, and 1 out of 54 fits for a decomposed mass model.

4.7 Subhalo scanning using different mass models

We now consider what impact assuming a different mass model has. The log evidence increase for the BPL, PL with multipoles and decomposed mass models, including a DM subhalo, are denoted $\Delta \ln \mathcal{Z}^{\rm BPL}$, $\Delta \ln \mathcal{Z}^{\rm Multipole}$, and $\Delta \ln \mathcal{Z}^{\rm Decomp}$, respectively.

There are four lenses where a PL mass model favours a DM subhalo ($\Delta \ln \mathcal{Z}^{\rm Source} > 10$) but at least one of the more complex mass models does not and the final DM subhalo inference disfavours a DM subhalo ($\Delta \ln \mathcal{Z}^{\rm Final} < 10$). This occurs in one lens for the BPL mass model ($\Delta \ln \mathcal{Z}^{\rm Source} > 10$ and $\Delta \ln \mathcal{Z}^{\rm BPL} < 10$), in two lenses for the PL with internal multipoles ($\Delta \ln \mathcal{Z}^{\rm Source} > 10$ and $\Delta \ln \mathcal{Z}^{\rm Multipole} < 10$) and two lenses for the decomposed mass model ($\Delta \ln \mathcal{Z}^{\rm Source} > 10$ and $\Delta \ln \mathcal{Z}^{\rm Decomp} < 10$). These values sum to five because this occurs for two different mass models in the same lens.

For these four lenses, Table 4 shows the Bayesian evidence increase of the more complex mass models compared to the simpler PL, before a DM subhalo is added to both. For all four lenses this value is above 10, confirming that the more complex mass model fits the lens better. The DM subhalo favoured in these four lenses when assuming a PL mass model were therefore false positive, which fitting a more accurate lens mass model removed. They are labelled FP-PL, for 'false positive power law', in the final column of Tables 2 and 3.

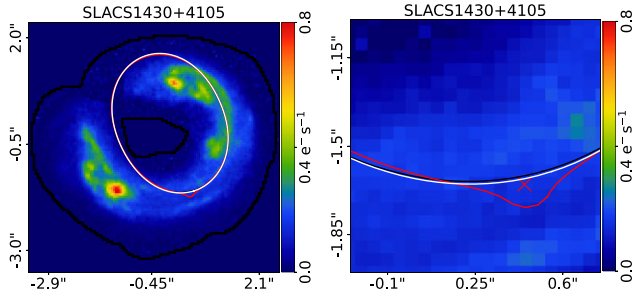

Figure 9. An attempt to visualize how making the lens mass model more complex may remove a DM subhalo candidate, illustrated using the lens SLACS1430 + 4105. The PL plus shear mass model gives $\Delta \ln \mathcal{Z}^{\rm Source} = 13.40$, compared to $\Delta \ln \mathcal{Z}^{\rm Decomp} = 6.54$ for a decomposed mass model which models separately the stellar and dark components. Both panels show the observed image, including the critical curves of the PL plus shear mass model without a DM subhalo (inner ellipse), with a DM subhalo (outer ellipse), and the decomposed mass model without a DM subhalo (middle ellipse). The right panel zooms-in on the location where the PL plus shear model favours a DM subhalo (cross). Including a DM subhalo or fitting a decomposed mass model expands the critical curves outwards in the same direction, albeit the decomposed model expands to a much lesser degree.

We looked for a visual indicator to explain why the more complex mass models removes the DM subhalo detection. Fig. 9 shows an attempt to do this using the lens SLACS1430 + 4105, where the simpler PL mass model favours a DM subhalo ($\Delta \ln \mathcal{Z}^{\rm Source} = 13.40$) but the more complex decomposed model does not ($\Delta \ln \mathcal{Z}^{\rm Decomp} = 6.54$). Fig. 9 shows that the decomposed mass model infers a tangential critical curve (white line) which is slightly extended outwards

Table 5. The inferred DM subhalo masses, $\log_{10}[M_{200}^{\rm sub}/{\rm M}_\odot]$, for the five lenses in the 'Cand' category. Masses are shown for the BPL, PL with multipoles, and decomposed mass models, which all include an external shear. Masses are shown for the models where a DM subhalo is favoured above our criteria of $\Delta \ln \mathcal{Z} > 10$. Errors quoted on $\log_{10}[M_{200}^{\rm sub}/{\rm M}_\odot]$ are at 3σ confidence.

Lens name	BPL	PL with multipoles	Decomposed
SLACS0946 + 1006	$8.62^{+2.15}_{-2.54}$	$10.37^{+0.80}_{-0.51}$	$10.37^{+0.80}_{-0.51}$
SLACS0029-0055	$10.03^{+0.03}_{-0.03}$		$10.03^{+0.03}_{-0.03}$
SLACS1029 + 0420			$9.05^{+2.57}_{-3.04}$
BELLS1226 + 5457	$11.67^{+0.18}_{-0.37}$	$11.48^{+0.16}_{-0.35}$	$10.96^{+0.27}_{-0.15}$
BELLS1201 + 4743	$11.23^{+0.12}_{-0.20}$		

compared to the PL mass model (black line). When a DM subhalo is included with the PL (red line), the tangential critical curve extends outwards in the same direction as the decomposed model, albeit to a much larger degree. Adding a DM subhalo to the decomposed model has a negligible impact on the tangential critical curve (not shown for visual clarity). Adding a DM subhalo to the simpler PL model and fitting a decomposed mass model (which is favoured by the Bayesian evidence overall) therefore produce stretching of the tangential critical curve in the same direction. They therefore both change the ray-tracing around the location the DM subhalo is detected, possibly explaining why it produces a a false positive for the PL, but it is certainly not conclusive.

There are two lenses where the PL mass model disfavoured a DM subhalo ($\Delta \ln \mathcal{Z}^{\rm Source} < 10$), but the decomposed mass model favoured one ($\Delta \ln \mathcal{Z}^{\rm Decomp} > 10$) and a DM subhalo was favoured overall across all mass models ($\Delta \ln \mathcal{Z}^{\rm Final} > 10$). These lenses are SLACS0029 − 0055 and SLACS1029 + 0420 are both assigned as candidate DM subhaloes and we discuss these lenses in detail in Section 5.

There are eight lenses where the PL model disfavoured a DM subhalo ($\Delta \ln \mathcal{Z}^{\rm Source} < 10$) but at least one of the more complex mass models favoured one. However, in these eight lenses, a DM subhalo was not favoured overall ($\Delta \ln \mathcal{Z}^{\rm Final} < 10$). This occurred once for the BPL, five times for the PL with internal multipoles and four times for the decomposed mass model. For these lenses, the PL without a DM subhalo had higher values of $\ln \mathcal{Z}$ than the more complex mass models with or without a DM subhalo. These eight lenses highlight that fitting a mass model which is too complex to be justified given the data quality may also produce false positive DM subhalo detections.

The inferred DM subhalo masses for the candidate strong lenses are given in Table 5.

4.8 Line-of-sight galaxies

We now consider whether including line-of-sight galaxies in the lens model changes the DM subhalo inference, by inspecting results for the PL plus shear mass model with line-of-sight galaxies included (see Section 3.3.6). We first isolate all lenses where the PL with line-of-sight galaxies was favoured over all other mass models, by finding those where their $\ln \mathcal{Z}$ value is above 10 any of the other four mass models. There are three lenses where this is the case: BELLS0113 + 0250, BELLS2342 − 0120, and BELLS1226 + 5457.

BELLS0113 + 0250 and BELLS2342 − 0120 are two of the lenses shown in Fig. 2, which were judged to have nearby line-of-sight galaxies just outside the lensed source. For both lenses, including line-of-sight galaxies notably impacts the DM subhalo inference. For BELLS2342 − 0120, the highest evidence mass model not including line-of-sight galaxies is the BPL. It gives $\ln \mathcal{Z} = 4588.00$ without a DM subhalo and $\ln \mathcal{Z} = 4601.19$ with a DM subhalo, meaning we would favour a DM subhalo. However, the PL with line-of-sight galaxies not including a DM subhalo has an even higher evidence ($\ln \mathcal{Z} = 4601.68$), meaning that we ultimately disfavour a DM subhalo. For BELLS0113 + 0250, ignoring the model with line of galaxies means we would infer $\Delta \ln \mathcal{Z} = 8.55$, which reduces to $\Delta \ln \mathcal{Z} = -0.17$ when considering the model with line-of-sight galaxies.

There are nine lenses where $\Delta \ln \mathcal{Z}^{\rm Los} > 10$, meaning that the PL with line-of-sight galaxies favours a DM subhalo. Four of these lenses are candidate subhaloes. Two lenses belong to the FP-PL category, meaning the model favouring a DM subhalo is likely a false positive due to the PL being too simple. The remaining three lenses are examples where fitting a mass model which is too complex to be justified given the data quality can give a spurious DM detection. There are 42 lenses remaining where the inclusion of line-of-sight galaxies had no impact on the DM subhalo inference. This includes three lenses in Fig. 2, which were judged to have nearby line-of-sight galaxies just outside the lensed source.

5 DISCUSSION

5.1 Expected detections

We now estimate upper limits on the number of expected DM subhalo detections for a ΛCDM Universe, via the sensitivity analysis performed in Amorisco et al. (2022) and He et al. (2022). Using PYAUTOLENS, these works simulated realizations of strong lens images which included subhaloes, with varying image-plane positions and masses, and quantified how detectable they are. Both works assumed parametric (cored) Sérsic sources, whereas this work uses Voronoi mesh source reconstructions. Using parametric sources makes subhaloes more detectable, therefore the expectations provided by these sensitivity maps are upper limits and this work should detect fewer DM subhaloes in a CDM universe. We quote values from their work where the threshold for a detection is consistent with ours, a log Bayesian evidence difference of 10.

We first consider what is the lowest detectable DM subhalo mass our fits are sensitive to. Amorisco et al. (2022) find that for *HST*-like data at a lensed source S/N (signal-to-noise ratio) of ∼50 we are sensitive to DM subhaloes of at least $10^{9.0}$ $\rm M_\odot$. Extrapolations of forecasts in He et al. (2022) indicate that DM subhaloes of masses $10^{9.0}$ $\rm M_\odot$ are detectable. These are consistent with sensitivity mapping performed by Despali et al. (2022) using a different lens modelling code (for a threshold $\Delta \ln \mathcal{Z} = 10.0$). The lowest detectable mass depends critically on the source S/N, and for many lenses our source S/N is below 50, meaning their lowest detectable mass will be above $10^{9.0}$ $\rm M_\odot$. However, the majority of detections listed in Tables 2 and 3 are above masses of $10^{10.0}$ $\rm M_\odot$. The masses of the candidate DM subhaloes are therefore feasible for our *HST* data.

We now consider upper limits on the expected number of detections for subhaloes between masses of $10^{10.0}$ and $10^{11.0}$ $\rm M_\odot$ in a CDM universe. At higher masses, their reduced number counts means that the random chance of alignment drives the probability of detection, as opposed to data quality. For a sample with lens redshift $z_{\rm lens} = 0.2$ and source redshift $z_{\rm src} = 0.6$, Amorisco et al. (2022) predict that there should be 0.025 detections per lens for subhaloes in the mass range 10^{10-11} $\rm M_\odot$ in the CDM case. For higher lens and

source redshifts, the expected number of detections rises up to 0.1. They do not provide forecasts for masses above $10^{11.0}$ $M_{\odot}$, but the rarity of these objects means they would not significantly change expectations.

For the simple lens model fitted in Section 4.2, which do not address false positives due to the lens light and source resolution, if we consider every candidate detection with an inferred mass above 10^{10} $M_{\odot}$ this gives a rate of 13 out of 37 or 0.351 detections per lens for SLACS and 7 out of 16 or 0.4375 detections per lens for BELLS-GALLERY. Systematic associated with the double Sérsic lens light model, low-resolution source, and PL plus shear mass model therefore led us to detect many more higher mass DM subhaloes than expected in CDM. After improving the lens and source models we were left with five DM subhalo candidates, a number which does not exceed CDM expectations.

5.2 Are any DM subhalo candidates genuine?

A key result of this paper is that changing the lens galaxy mass model changes the DM subhalo inference. For example, we identified 4 out of 54 lenses where a PL mass model produces a false positive removed by a more complex mass model (category 'FP-PL') and two lenses where a decomposed mass model favours a DM subhalo when other models did not (category 'Decomp'). Only 2 out of 54 lenses favoured a DM subhalo for all five mass models fitted. We cannot ascertain whether any DM subhalo candidate is genuine – even for these two lenses, we cannot be certain whether another hypothetical mass model not fitted in this work would remove the DM subhalo detection.

To determine if they are genuine we must apply the technique used in other studies (Koopmans 2005; Vegetti & Koopmans 2009; Ritondale et al. 2019b; Vernardos & Koopmans 2022), where free-form pixelized corrections are added to the lens's gravitational potential. This confirms a DM subhalo candidate is genuine by requiring that these corrections reconstruct a *local* 2D overdensity in the lens's convergence, that is consistent with the parametric DM subhalo inferred via lens modelling. In many lenses, the corrections produce *global* changes to the convergence, indicating that a DM subhalo candidate is actually accounting for a systematic in the lens model. Future work will assess our DM subhalo candidates using this technique.

Whilst our study cannot determine if any DM subhalo candidates are genuine, by considering the DM subhalo inferences for different mass models we can gain insight on DM subhalo strong lens analysis. We therefore now consider in detail the different assumptions made by the different mass models and relate this to how it changes our DM subhalo results.

5.3 Removing DM subhalo candidates with a more complex mass model

We showed evidence of four lenses (see Table 4) where fitting a more complex mass model (either a PL with multipoles or decomposed mass model) did not favour a DM subhalo when the simpler PL model did. In all four lenses, the inferred Bayesian evidence for the more complex mass model was above that of the PL (both without a DM subhalo) by over 10. These four lenses make up the category FP-PL for 'false positive power law'.

The cause of this behaviour is illustrated in He et al. (2023, hereafter H23) using *HST*-like strong lens images simulated via a high-resolution zoom-in cosmological simulation (Richings et al. 2021) of a massive elliptical galaxy. H23 showed that a mismatch between the assumed lens mass model and the simulated lens galaxy's more complex underlying mass distribution could create a signal that resembles the perturbing effect of a DM subhalo. In certain simulated datasets, where a DM subhalo was not truly present, the lens model favoured a DM subhalo with an increase of log evidence of up to 30. The PL favoured a DM subhalo for all five lenses in the FP-PL category with $\Delta \ln \mathcal{Z}^{\rm Source} \simeq 30$ or less.

Two of these lenses, SLACS1250 − 0523 and SLACS1430 + 4105, were in the sample of three lenses studied by Nightingale et al. (2019). The authors showed that the stellar mass distribution of both lenses are composed of two elliptical components with unique axis ratios and position angles. When the authors fitted an SIE mass model to SLACS1430 + 4105 its inferred position angle went to a value between those inferred for each Sérsic. They argued that the SIE model therefore adjusted its orientation to try and capture the lens's true complexity, which is captured by the decomposed mass model. Their study supports the argument that these two lenses have the type of complex features in their mass distribution which H23 showed cause false positive DM subhalo detections. Work by Vegetti et al. (2014) also did not favour a DM subhalo in SLACS1430 + 4105, supporting the false positive interpretation.

Fitting more complex mass models can therefore remove false positives by adding complexity that is present in the lens's true mass distribution. Therefore, in 4 out of 54 lenses, or 7.4 per cent of our sample, the PL mass model produces false positive DM subhalo detections. Amongst these four lenses, the BPL removes one false positive, the PL plus multipoles removes two and the decomposed mass model removes two.

5.4 Creating DM subhalo candidates with a decomposed mass model

In Appendix B, we showed that the PL lens mass model 'absorbed' genuine DM subhalo signals by adjusting the inferred mass model parameters away from their true input values. For the decomposed mass model, the centres, axis ratios, and position angles of the two Sérsic components representing the decomposed model's stellar mass are tied to that of the lens galaxy's light (each Sérsic component has mass-to-light ratio and gradient parameters that are free to vary). The restrictions this puts on the lens's 2D stellar mass distribution therefore may reduce this subhalo absorption effect and make DM subhaloes not detected with the PL model detectable.

This is a plausible interpretation of the results for the lenses SLACS0029 − 0055 and SLACS1029 + 0420, where a PL mass model did not favour a DM subhalo but the decomposed mass model did, with values of $\Delta \ln \mathcal{Z}^{\rm Final} = 23.69$ and 10.57, respectively. However, we cannot be certain that the linking of light to mass in the decomposed mass model is a robust assumption. The decomposed mass model could be creating a false positive due to some form of missing complexity, in a similar fashion seen for the four lenses discussed above. Fitting a decomposed mass model, which better captures the lens's true mass distribution, may therefore make DM subhaloes detectable which are not detectable when fitting other lens mass models. Future work will test this hypothesis by applying the potential corrections described in Section 5.2 to these two lenses.

5.5 What mass model complexity is missing?

The FP-PL category consists of four lenses where a DM subhalo was favoured for the PL model and disfavoured for the PL with multipoles or decomposed mass model, and the latter had a higher

overall evidence. When comparing to the BPL instead of the PL, the results do not change for any of these lenses. The multipoles and decomposed mass models are therefore adding a form of complexity, not present in the PL or BPL, which removes DM subhalo candidates. These models add complexity to the mass distribution's angular structure, for example, allowing azimuthal variations in the projected density that vary with radius. In contrast, the BPL only adds freedom radially. This is evidence that it is missing complexity in the angular structure of lens mass models which creates false positives DM subhalo candidates. This is consistent with H23 and is discussed by Kochanek (2021) in the context of measuring the *Hubble* Constant with strong lenses.

Of these four lenses, there are two where the PL with multipoles changed the DM inference and two where it was the decomposed mass model. The PL with multipoles and decomposed mass models therefore do not always give consistent DM subhalo results, because they add angular structure to the mass distribution in different ways. The fourth order multipole fitted in this work adds boxiness/disciness to the mass distribution (Van De Vyvere et al. 2022b), whereas the decomposed mass model allows for mass twists and departures from a single axis ratio (Nightingale et al. 2019).

Studies of local massive elliptical galaxies have revealed a diversity of complex structures, including kinematically distinct cores (Krajnović et al. 2011), boxy/discy isophotes (Emsellem et al. 2011), isophotal twists, and centre shifts (Goullaud et al. 2018). Recent works have investigated what impact these have on lens models (Cao et al. 2021; Van De Vyvere et al. 2022a, b; Etherington et al. 2023b). Edge-on discs have also been shown to cause false positive DM signals (Hsueh et al. 2016, 2017, 2018). These forms of complexity add smoothly changing radial and azimuthal features to the mass distribution, which the BPL, PL with multipoles, and decomposed models add in different ways.

Our results motivate the development of more complex mass models that add azimuthal freedom (and to a lesser degree, radial freedom) in a way that captures the true complexity of all lens galaxies. However, it is unclear how. Evaluating a mass model's deflection angles typically relies on it conforming to elliptical symmetry (e.g. that all iso-convergence contours correspond to a single position angle and axis ratio). Even if we are able to determine what complexity is missing from the mass model, it remains to be seen whether one can practically fit it as a parametrized lens mass model. Future work will build-on the results of this study in order to better understand what mass model complexity is missing.

5.6 Potential corrections

The potential corrections technique (Koopmans 2005; Vegetti & Koopmans 2009; Suyu et al. 2010; Vernardos & Koopmans 2022) can provide key insight on the missing mass model complexity (Powell et al. 2022). Performing the potential corrections analysis (see Section 5.2) for different mass models and comparing the results will facilitate progress, because the complexity included and omitted should be reflected in the potential corrections themselves.

This raises an important question, how well do the potential corrections perform in a regime where a DM subhalo is present, but there is also missing complexity in the lens mass model? In this scenario, the lensing signal produced by a DM subhalo will be superimposed with the signal produced by missing complexity in the lens mass model. Would the potential corrections reproduce the local DM subhalo signal and simultaneously correct the mass model on a global scale, or would a degenerate solution be inferred such that the DM subhalo is rejected? This scenario is considered by Galan et al. (2022) who use wavelets to perform a multiscale potential correction on simulated lenses. Their analysis indicates the signals are separable because they operate on different physical scales.

5.7 What about line-of-sight galaxies?

There are two lenses where including line-of-sight galaxies had a meaningful impact on the DM subhalo inference, both of which had bright galaxies within $\sim$1.0 arcsec of the lensed source. There are three more lenses which had bright galaxies this close, but their inclusion did not change the DM subhalo inference. For the remaining 49 lenses, models including line-of-sight galaxies were fitted, but these objects were typically $\sim$3.0 arcsec or more from the lens and relatively faint. Provided line-of-sight galaxies are sufficiently far from the lens they therefore do not impact the DM subhalo inference, at least for *HST* quality data. Future work could quantify this more precisely, by estimating the masses of the line-of-sight galaxies from their luminous emission.

5.8 Subhalo masses

H23 show that an overly simplistic mass model can lead to overestimates of $M_{200}^{\rm sub}$ by a factor of $\sim$4. Given the uncertainty surrounding whether our DM subhalo candidates are genuine, interpreting their inferred masses, which are given in Table 5, is difficult. We therefore focus on SLACS0946 + 1006, a confirmed DM subhalo (Vegetti et al. 2010), which passed our detection criteria for all mass models (category A). Our 3σ confidence intervals for $M_{200}^{\rm sub}$ – with each of the different lens mass models (which all include an external shear) – are:

(i) PL: $M_{200}^{\rm sub} = 1.00^{+0.32}_{-0.25} \times 10^{11} {\rm M}_{\odot}$,
(ii) BPL: $M_{200}^{\rm sub} = 3.42^{+2.61}_{-1.93} \times 10^{11} {\rm M}_{\odot}$,
(iii) PL with multipoles: $M_{200}^{\rm sub} = 2.51^{+1.71}_{-1.1} \times 10^{11} {\rm M}_{\odot}$,
(iv) Decomposed mass model: $M_{200}^{\rm sub} = 0.85^{+0.87}_{-0.59} \times 10^{11} {\rm M}_{\odot}$,
(v) PL with line-of-sight galaxies: $M_{200}^{\rm sub} = 2.53^{+3.72}_{-1.77} \times 10^{11} {\rm M}_{\odot}$.

The $M_{200}^{\rm sub}$ estimates therefore vary depending on the mass model, with the BPL value inconsistent with the PL. We anticipate that attempts to constrain more subtle DM properties like the subhalo's concentration will be more impacted by this degeneracy with the lens mass model (Minor et al. 2021b). Understanding the missing complexity in strong lens mass models is important for ensuring that DM subhalo mass measurements are accurate.

Even if our mass models were perfect, the mass estimates quoted in this work for any genuine DM subhalo have additional potential systematics. Our DM subhalo model assumes they lie on the mass-concentration relation from Ludlow et al. (2016) and we will overestimate the mass of any genuine DM subhalo which is more concentrated than this relation (because more concentrated NFW haloes have a higher central density, making their perturbations to the lensing more prominent, see Amorisco et al. 2022). This is also shown by Minor et al. (2021a, b). DM subhaloes may also be at a different redshift to the lens, which can also lead to an incorrect mass estimate (Li et al. 2017; Despali et al. 2018, 2022; Amorisco et al. 2022; He et al. 2022).

5.9 Improving other aspects of lens models

The evidence favouring a DM subhalo decreased by more than 10 when: (i) residuals from an inadequate lens light subtraction were removed in 12 out of 54 lenses; and (ii) the source reconstruction resolution was increased in 7 out of 54 lenses. We identified this

by refitting each lens with simple changes to the imaging data and masks, similar to those used by other studies (Vegetti et al. 2014; Ritondale et al. 2019b). Improving PYAUTOLENS to mitigate these systematics is also straightforward, for example, using more flexible lens light models (e.g. basis functions; Tagore & Jackson 2016) and optimizing the code to reconstruct sources at higher resolution.

5.10 Comparison with other works

We now compare to studies by Vegetti et al. (2010, 2014) and Ritondale et al. (2019b) who search for subhaloes in the SLACS and BELLS-GALLERY samples. These works use lens light subtracted images, source-only masks, and a PL mass model, thus our $\Delta \ln \mathcal{Z}^{\rm Source}$ values are the most suitable to compare. In certain lenses these studies include line-of-sight galaxies, meaning that we compare $\Delta \ln \mathcal{Z}^{\rm Los}$ values.

Vegetti et al. (2010) present the detection of a DM subhalo in the lens system SLACS0946 + 1006, for which we infer $\Delta \ln \mathcal{Z}^{\rm Source} = 72.36$ and assign it as a DM subhalo candidate. Our inferred values of $(x, y) = (-1.22, -1.28)$ are consistent with the values presented in Vegetti et al. (2010). Comparing subhalo mass is less straightforward, because Vegetti et al. (2010) assume a pseudo-Jaffe density profile whereas we assume an NFW. The pseudo-Jaffe parametrization is more centrally dense than the NFW, such that a factor of ∼10 difference is expected between their inferred masses (Vegetti et al. 2018). The mass of $M_{200}^{\rm sub} = 1.00^{+0.32}_{-0.25} \times 10^{11}\,{\rm M}_{\odot}$ for our NFW subhalo model is therefore qualitatively above what one would have predicted by converting their pseudo-Jaffe inferred value of $3.51 \times 10^{9}\,{\rm M}_{\odot}$ to an NFW. Our results therefore agree with Vegetti et al. (2010).

Vegetti et al. (2014) analyse the following 11 SLACS lenses: SLACS0252+0039, SLACS0737+3216, SLACS0956+5100, SLACS0959+4416, SLACS1023+4230, SLACS1205+4910, SLACS1430+4105, SLACS1627 − 0053, SLACS2238 − 0754, and SLACS2300+0022. They report no DM substructure detection for every system. All of these lenses are in our SLACS sample except SLACSJ0959 + 4416, which we removed due to a poor lens light subtraction. Our highest $\Delta \ln \mathcal{Z}^{\rm Source}$ value for a lens in common with this sample (omitting SLACS0946+1006) is SLACS0956 + 5100 with a value of $\Delta \ln \mathcal{Z}^{\rm Source} = 23.35$. We infer $\Delta \ln \mathcal{Z}^{\rm Source} > 10$ for one more shared lens, SLACS1430 + 4105. To claim a DM subhalo detection, Vegetti et al. (2014) require that the Bayesian evidence increases by 50. Therefore, for all 10 overlapping lenses we are in agreement.

Ritondale et al. (2019b) analyse 17 lenses from the BELLS-GALLERY sample, of which 16 are shared with our sample (we removed a system with two lens galaxies). In three lenses they find that the addition of a subhalo in the lens model increases the Bayesian evidence by more than 100; BELLS0742 + 3341, BELLS0755 + 3445, and BELLS1110 + 3649. For these three lenses, we infer $\Delta \ln \mathcal{Z}^{\rm Source}$ values of −3.59, 1268.78, and 12.65, respectively. We attribute BELLS0755 + 3445 as a catastrophic failure and Ritondale et al. (2019b) specifically discuss this as a lens with an inaccurate mass model that causes a spurious DM subhalo inference. We find $\Delta \ln \mathcal{Z}^{\rm Source} > 100.0$ in three more lenses which we class as catastrophic failures, BELLS0918 + 5104, BELLS0029 + 2544, and BELLS0201 + 32284, which are not mentioned specifically by Ritondale et al. (2019b). In the lens BELLS1226 + 5457, we infer $\Delta \ln \mathcal{Z}^{\rm Source} = 105.90$, which is reported below 100 in Ritondale et al. (2019b).

There are differences between our results and those of Ritondale et al. (2019b). Assessing the cause for discrepancy is difficult. BELLS-GALLERY source galaxies are compact Lyman-α emitters (Shu et al. 2016; Ritondale et al. 2019a) which for fits to simulated lenses with similar source properties highlighted the need for higher source resolution (see Appendix B4). Therefore the differences are likely due to how each work approaches the source analysis. Although PYAUTOLENS and the method of Ritondale et al. (2019b) are similar, there are differences in their implementation and the regularization schemes that are applied. More detailed study is warranted, especially in light of the systematics highlighted by Etherington et al. (2022) where stochasticity in the construction of the source can produce large spikes in the log likelihood.

6 SUMMARY

In this work, we scan for DM subhaloes in 54 strong lenses imaged by the *HST*: twice as many as have been previously attempted (Vegetti et al. 2014; Ritondale et al. 2019b). To achieve this, we successfully developed a predominantly automated data processing pipeline, based on open-source lens modelling software PYAUTOLENS. By comparing lens models with and without DM subhaloes, we infer the probability that each lens contains a DM substructure. Tested on idealized mock *HST* images of 16 lenses, our method correctly identifies DM substructures of mass $>10^{9.5}\,{\rm M}_{\odot}$ (the expected sensitivity of *HST*, Amorisco et al. 2022; Despali et al. 2022; He et al. 2022) without false positives, provided that the source galaxy reconstruction has sufficiently high resolution.

We identify five DM subhalo candidates, including one previously identified in the lens SLACS0946 + 1006 (Vegetti et al. 2010). For two candidates fits using simpler models for the lens's mass did not favour a DM subhalo, but more complex mass models which use separate components for the stars and DM do. Future work will extend these fits using a pixel-grid-based technique for the lens's gravitational potential (Koopmans 2005; Vegetti & Koopmans 2009), in order to definitively determine whether any of these candidates are genuine DM subhalo detections. We identify a total of 45 non-detections, which are vital for overcoming Poisson statistics when constraining DM models (Despali et al. 2022).

We demonstrate that changing the complexity of the lens galaxy's mass model has a dramatic impact on the DM subhalo inference. Because our software is highly automated, we have been able to fit five different parametric forms for the lens's mass which are used in the literature: (i) PL (Tessore & Metcalf 2015); (ii) BPL (O'Riordan et al. 2019, 2020, 2021); (iii) PL including internal multipoles (Chu et al. 2013); (iv) decomposition of the lens into stellar and dark components (Nightingale et al. 2019) and; (v) a PL where the mass of nearby line-of-sight galaxies is also accounted for. An external shear term is included in all models.

We demonstrate that fits assuming a more complex model for the lens's mass distribution may: (i) favour the inclusion of a DM subhalo when fits assuming a simpler lens mass model do not (2 out of 54 lenses) and; (ii) remove false positive DM subhalo detections found when assuming a simpler lens mass model (6 out of 54 lenses). The inferred DM subhalo masses also depend on the mass model that we assume.

We believe that the main form of complexity missing in our lens mass models was in their azimuthal structure, and that effort must be placed on developing lens models that add this. If done correctly, the pay-off could be huge – enabling studies that are more sensitive to DM subhaloes of lower masses than previously forecasted and which are devoid of false positive detections.

The importance of automating strong lensing analysis will increase in future surveys. Several hundred lenses will be required for

competitive constraints on DM physics (Vegetti et al. 2018; Amorisco et al. 2022; Despali et al. 2022; He et al. 2022); and thousands (or tens of thousands) of lenses will soon be discovered by the *James Webb Space Telescope*, *Euclid*, and *Roman Space Telescopes* (Collett 2015). These exquisite data sets and large lens samples will allow us to test ΛCDM on smaller scales of the Universe than ever before.

SOFTWARE CITATIONS

This work uses the following software packages:

(i) PYAUTOFIT (Nightingale et al. 2021b).
(ii) PYAUTOGALAXY (Nightingale et al. 2023a).
(iii) PYAUTOLENS (Nightingale & Dye 2015; Nightingale et al. 2018, 2021b).
(iv) ASTROPY (Astropy Collaboration 2013; Price-Whelan et al. 2018).
(v) COLOSSUS (Diemer 2018).
(vi) CORNER.PY(Foreman-Mackey 2016).
(vii) DYNESTY (Speagle 2020).
(viii) MATPLOTLIB(Hunter 2007).
(ix) NUMBA (Lam, Pitrou & Seibert 2015).
(x) NUMPY (van der Walt, Colbert & Varoquaux 2011).
(xi) PYTHON (Van Rossum & Drake 2009).
(xii) SCIKIT-IMAGE (Van der Walt et al. 2014).
(xiii) SCIKIT-LEARN (Pedregosa et al. 2011).
(xiv) SCIPY (Virtanen et al. 2020).
(xv) SQLITE (Hipp 2020).

ACKNOWLEDGEMENTS

JWN is supported by the UK Space Agency, through grant ST/N001494/1, and a Royal Society Short Industry Fellowship. AE is supported by STFC via grants ST/R504725/1 and ST/T506047/1. AA, SC, CSF, and QH acknowledge support from the European Research Council (ERC) through Advanced Investigator grant DMIDAS (GA 786910). XYC and RL acknowledge the support of the National Nature Science Foundation of China (nos 11988101, 11773032, and 12022306), the support from the Ministry of Science and Technology of China (grant nos 2020SKA0110100), the science research grants from the China Manned Space Project (nos CMS-CSST-2021-B01 and CMS-CSST-2021-A01), CAS Project for Young Scientists in Basic Research (no. YSBR-062), and the support from K. C. Wong Education Foundation.

This work used both the Cambridge Service for Data Driven Discovery (CSD3) and the DiRAC Data-Centric system, project code dp195, which are operated by the University of Cambridge and Durham University on behalf of the STFC DIRAC HPC Facility (www.dirac.ac.uk). These were funded by BIS capital grant ST/K00042X/1, STFC capital grants ST/P002307/1, ST/R002452/1, ST/H008519/1, ST/K00087X/1, STFC Operations grants ST/K003267/1, ST/K003267/1, and Durham University. DiRAC is part of the UK National E-Infrastructure.

DATA AVAILABILITY

Analysis results are publically available at https://github.com/Jammy2211/autolens_subhalo.

REFERENCES

Ade P. A. et al., 2016, A&A, 594, A13
Amorisco N. C. et al., 2022, MNRAS, 510, 2464
Anderson L. et al., 2014, MNRAS, 441, 24
Astropy Collaboration, 2013, A&A, 558, A33
Belokurov V., Irwin M. J., Koposov S. E., Evans N. W., Gonzalez-Solares E., Metcalfe N., Shanks T., 2014, MNRAS, 441, 2124
Benitez-Llambay A., Frenk C., 2020, MNRAS, 13, 1
Bode P., Ostriker J. P., Turok N., 2001, ApJ, 556, 93
Bolton A. S., Burles S., Koopmans L. V. E., Treu T., Gavazzi R., Moustakas L. A., Wayth R., Schlegel D. J., 2008, ApJ, 682, 964
Cao X. et al., 2021, Res. Astron. Astrophys., 22, 30
Chu Z., Lin W. P., Li G. L., Kang X., 2013, ApJ, 765, 134
Ciotti L., Bertin G., 1999, A&A, 352, 447
Collett T. E., 2015, ApJ, 811, 20
Cornachione M. A. et al., 2018, ApJ, 853, 148
Despali G., Vegetti S., 2017, MNRAS, 469, 1997
Despali G., Vegetti S., White S. D., Giocoli C., van den Bosch F. C., 2018, MNRAS, 475, 5424
Despali G., Vegetti S., White S. D., Powell D. M., Stacey H. R., Fassnacht C. D., Rizzo F., Enzi W., 2022, MNRAS, 510, 2480
Diemand J., Kuhlen M., Madau P., 2007, ApJ, 667, 859
Diemand J., Kuhlen M., Madau P., Zemp M., Moore B., Potter D., Stadel J., 2008, Nature, 454, 735
Diemer B., 2018, ApJS, 239, 35
Dye S., Evans N. W., Belokurov V., Warren S. J., Hewett P., 2008, MNRAS, 388, 384
Elson R. A. W., Fall S. M., Freeman K. C., 1987, ApJ, 323, 54 (EFF)
Emsellem E. et al., 2011, MNRAS, 414, 888
Enzi W. et al., 2021, MNRAS, 506, 5848
Etherington A. et al., 2022, MNRAS, 517, 3275 (E22)
Etherington A. et al., 2023a, preprint (arXiv:2301.05244)
Etherington A. et al., 2023b, MNRAS, 521, 6005
Foreman-Mackey D., 2016, J. Open Source Softw., 1, 24
Galan A., Vernardos G., Peel A., Courbin F., Starck J.-L., 2022, A&A, 668, 24
Goullaud C. F., Jensen J. B., Blakeslee J. P., Ma C.-P., Greene J. E., Thomas J., 2018, ApJ, 856, 11
He Q. et al., 2022, MNRAS, 512, 5862
He Q. et al., 2023, MNRAS, 518, 220 (H23)
Hezaveh Y. D. et al., 2016, ApJ, 823, 37
Hildebrandt H. et al., 2017, MNRAS, 465, 1
Hipp R. D., 2020, SQLite, available at: https://www.sqlite.org/index.html
Hsueh J. W., Fassnacht C. D., Vegetti S., McKean J. P., Spingola C., Auger M. W., Koopmans L. V., Lagattuta D. J., 2016, MNRAS, 463, L51
Hsueh J. W. et al., 2017, MNRAS, 469, 3713
Hsueh J. W., Despali G., Vegetti S., Xu D., Fassnacht C. D., Metcalf R. B., 2018, MNRAS, 475, 2438
Hunter J. D., 2007, Comput. Sci. Eng., 9, 90
Kochanek C. S., 2021, MNRAS, 501, 5021
Koopmans L. V., 2005, MNRAS, 363, 1136
Krajnović D. et al., 2011, MNRAS, 414, 2923
Lam S. K., Pitrou A., Seibert S., 2015, Proceedings of the Second Workshop on the LLVM Compiler Infrastructure in HPC—LLVM'15. p. 1
Li R., Frenk C. S., Cole S., Gao L., Bose S., Hellwing W. A., 2016, MNRAS, 460, 363
Li R., Frenk C. S., Cole S., Wang Q., Gao L., 2017, MNRAS, 468, 1426
Ludlow A. D., Bose S., Angulo R. E., Wang L., Hellwing W. A., Navarro J. F., Cole S., Frenk C. S., 2016, MNRAS, 460, 1214
Maresca J., Dye S., Li N., 2021, MNRAS, 503, 2229
McKean J. et al., 2015, in Advancing Astrophysics with the Square Kilometre Array (AASKA14). p. 84, preprint (arXiv:1502.03362)
Minor Q., Kaplinghat M., Chan T. H., Simon E., 2021a, MNRAS, 507, 1202
Minor Q., Gad-Nasr S., Kaplinghat M., Vegetti S., 2021b, MNRAS, 507, 1662
Navarro J. F., Frenk C. S., White S. D. M., 1996, ApJ, 462, 563
Navarro J. F., Frenk C. S., White S. D. M., 1997, ApJ, 490, 493
Nightingale J. W., Dye S., 2015, MNRAS, 452, 2940
Nightingale J. W., Dye S., Massey R. J., 2018, MNRAS, 478, 4738

Nightingale J. W., Massey R. J., Harvey D. R., Cooper A. P., Etherington A., Tam S. I., Hayes R. G., 2019, MNRAS, 489, 2049
Nightingale J., Hayes R., Griffiths M., 2021a, J. Open Source Softw., 6, 2550
Nightingale J. et al., 2021b, J. Open Source Softw., 6, 2825
Nightingale J. W. et al., 2023a, J. Open Source Softw., 8, 4475
Nightingale J. W. et al., 2023b, MNRAS, 521, 3298
O'Riordan C. M., Warren S. J., Mortlock D. J., 2019, MNRAS, 487, 5143
O'Riordan C. M., Warren S. J., Mortlock D. J., 2020, MNRAS, 496, 3424
O'Riordan C. M., Warren S. J., Mortlock D. J., 2021, MNRAS, 501, 3687
Oguri M., 2021, PASP, 133, 6
Pedregosa F. et al., 2011, J. Mach. Learn. Res., 12, 2825
Powell D. M., Vegetti S., McKean J. P., Spingola C., Stacey H. R., Fassnacht C. D., 2022, MNRAS, 516, 1808
Price-Whelan A. M. et al., 2018, AJ, 156, 123
Richings J., Frenk C., Jenkins A., Robertson A., Schaller M., 2021, MNRAS, 501, 4657
Ritondale E., Auger M. W., Vegetti S., McKean J. P., 2019a, MNRAS, 482, 4744
Ritondale E., Vegetti S., Despali G., Auger M. W., Koopmans L. V., McKean J. P., 2019b, MNRAS, 485, 2179
Sawala T. et al., 2016, MNRAS, 456, 85
Seiler M. C., Seiler F. A., 1989, Risk Anal., 9, 415
Shi X., Fuller G. M., 1999, Phys. Rev. Lett., 82, 2832
Shu Y. et al., 2016, ApJ, 824, 86
Sibson R., 1981, Interpreting Multivariate Data. John Wiley and Sons, New York
Speagle J. S., 2020, MNRAS, 493, 3132
Springel V. et al., 2005, Nature, 435, 629
Springel V. et al., 2008, MNRAS, 391, 1685
Suyu S. H., Marshall P. J., Hobson M. P., Blandford R. D., 2006, MNRAS, 371, 983
Suyu S. H., Marshall P. J., Auger M. W., Hilbert S., Blandford R. D., Koopmans L. V., Fassnacht C. D., Treu T., 2010, ApJ, 711, 201
Tagore A. S., Jackson N., 2016, MNRAS, 457, 3066
Tessore N., Metcalf R. B., 2015, A&A, 580, 1
van der Walt S., Colbert S. C., Varoquaux G., 2011, Comput. Sci. Eng., 13, 22
Van De Vyvere L., Sluse D., Gomer M. R., Mukherjee S., 2022a, A&A, 179, 1
Van De Vyvere L., Gomer M. R., Sluse D., Xu D., Birrer S., Galan A., Vernardos G., 2022b, A&A, 659, 1
Van Rossum G., Drake F. L., 2009, Python 3 Reference Manual. CreateSpace, Scotts Valley, CA
Vegetti S., Koopmans L. V., 2009, MNRAS, 392, 945
Vegetti S., Koopmans L. V., Bolton A., Treu T., Gavazzi R., 2010, MNRAS, 408, 1969
Vegetti S., Lagattuta D. J., McKean J. P., Auger M. W., Fassnacht C. D., Koopmans L. V., 2012, Nature, 481, 341
Vegetti S., Koopmans L. V., Auger M. W., Treu T., Bolton A. S., 2014, MNRAS, 442, 2017
Vegetti S., Despali G., Lovell M. R., Enzi W., 2018, MNRAS, 481, 3661
Vernardos G., Koopmans L. V. E., 2022, MNRAS, 516, 1347
Virtanen P. et al., 2020, Nat. Methods, 17, 261
Van der Walt S., Schönberger J. L., Nunez-Iglesias J., Boulogne F., Warner J. D., Yager N., Gouillart E., Yu T., 2014, PeerJ, 2, e453
Warren S., Dye S., 2003, ApJ, 590, 673
Zhao H., 1996, MNRAS, 278, 488

APPENDIX A: REGULARIZATION FORMALISM

The linear regularization matrix H used in Warren & Dye (2003) and Nightingale & Dye (2015) is derived following the formalism given in Seiler & Seiler (1989), where $\mathsf{H} = \mathsf{B}^T\mathsf{B}$ and the matrix B stores the regularization pattern of source pixels with one another. For example, to regularize a source pixel with its neighbour, assuming that pixel one is a neighbour of pixel two, and two of three, etc., the matrix $\mathsf{B_x}$ is given as

$$\begin{bmatrix} -1 & 1 & 0 & 0 & \dots \\ 0 & -1 & 1 & 0 & \dots \\ 0 & 0 & -1 & 1 & \dots \\ \dots & \dots & \dots & \dots & \dots \end{bmatrix}. \tag{A1}$$

For gradient regularization on an $N \times N$ square grid, this matrix gives the regularization of source pixels across the x-direction, where every N elements will be a row of zeros. This matrix then gives a regularization matrix $\mathsf{H_x} = \mathsf{B_x}^T\mathsf{B_x}$. For regularization in the y-direction, a second $\mathsf{B_y}$ matrix is generated, where the values of negative one are again across the diagonal and the values of positive ones are every N elements across from this, with the final N rows all zeros. $\mathsf{B_y}$ is then used to compute a second regularization matrix $\mathsf{H_y} = \mathsf{B_y}^T\mathsf{B_y}$, which is added to the first to give the overall regularization matrix $\mathsf{H} = \mathsf{H_x} + \mathsf{H_y}$. Gradient regularization used in this work follows the same pattern, but computes around 5–10 H matrices corresponding to regularization across all neighbouring Voronoi vertex indices.

DM subhalo results use a scheme which adapts the degree of smoothing to the reconstructed source's luminous emission. First, an estimate of the flux that will be reconstructed by each Voronoi cell is computed using a previous model of the lensed source emission, Ξ_j, as

$$v_\mathrm{i} = \frac{\sum_{\mathrm{k}=1}^{K} w\, \Xi_{\mathrm{Src,k}}}{K}, \tag{A2}$$

where the summation is over the K image pixels allocated to each Voronoi source pixel and w is given by equation (13). Each element in $\vec{v}$ is divided by K to normalize for the number of allocated image pixels, thereby ensuring that the source pixels which (by chance) are allocated more image pixels do not receive a higher value of v_i than those which are allocated fewer. The vector $\vec{V}$ is then computed, where each element is given by

$$V_\mathrm{i} = \left[\frac{v_\mathrm{i}}{v_\mathrm{max}}\right]^{L_\mathrm{Lum}}. \tag{A3}$$

Each element is divided by the maximum value of $\vec{v}$ to scale all values between zero and one and raised to the power of the hyperparameter L_Lum. $\vec{V}$ is then used to compute the luminosity-weighted regularization value of each source pixel as

$$\Lambda_\mathrm{i} = \lambda_\mathrm{Src} V_\mathrm{i} + \lambda_\mathrm{BG}(1 - V_\mathrm{i}), \tag{A4}$$

therefore leading to two regularization coefficients λ_Src and λ_BG, which are both free parameters.

To perform luminosity-weighted regularization, the 1D vector of regularization coefficients $\vec{\Lambda}$ (see equation A4) is folded into the computation of H. The $\vec{B}$ matrices above are redefined to include each pixel's effective regularization coefficient, λ_eff, as $\mathsf{B}_\Lambda = \vec{\Lambda}\mathsf{B}$, where $\vec{\Lambda}$ is given by equation (A4). The corresponding regularization matrix is then $\mathsf{H}_\Lambda = \mathsf{B}_\Lambda^T\mathsf{B}_\Lambda$.

We use the PYAUTOLENS regularization scheme `AdaptiveBrightnessSplit`. This scheme also regularizes the source pixel values by interpolating values at a cross of surrounding points, which depends on the size of each source pixel and is independent of the number of connecting neighbours between source pixels, which can be unstable. Explicitly, the regularization term of the `AdaptiveBrightnessSplit` is given by (following the expression

of Warren & Dye 2003)

$$G_L = \sum_{j=1}^{J} \{ \left[s_j - \tilde{s}\left(x_j + l_j,\ y_j + l_j\right) \right]^2 + \left[s_j - \tilde{s}\left(x_j - l_j,\ y_j + l_j\right) \right]^2 + \left[s_j - \tilde{s}\left(x_j + l_j,\ y_j - l_j\right) \right]^2 + \left[s_j - \tilde{s}\left(x_j - l_j,\ y_j - l_j\right) \right]^2 \}, \quad \text{(A5)}$$

where s_j is the value of the source pixel j (at position (x_j, y_j)). $\tilde{s}\,(x,\ y)$ is the natural neighbour interpolating function given by $\{s_j\}_{j=0}^{J}$. l_j is the Voronoi 'length' of the jth source pixel which is defined as the square root of the area of jth source pixel (Voronoi cell), A_j. With the expression of G_L, the regularization matrix H is then derived as (see eq. 13 of Warren & Dye 2003)

$$H_{i,j} = \frac{1}{2} \frac{\partial G_L}{\partial s_i \partial s_j}. \quad \text{(A6)}$$

This regularization scheme is similar to what is used in the work of Vegetti & Koopmans (2009). The difference is that Vegetti & Koopmans (2009) compute the difference between the value at a Delaunay vertex and the (barycentrically) interpolated values at associated intersecting points of horizontal (vertical) lines and Delaunay edges, while here we compute the value at a Voronoi vertex and the (natural neighbouring) interpolated values at positions separated by the associated Voronoi 'length'.

APPENDIX B: SIMULATED DATA RESULTS

B1 Simulations

We test our lens modelling and subhalo scanning pipelines on a sample of 16 simulated lenses. For every lens we assume a lens galaxy and subhalo (when included) at $z = 0.5$, and a source at $z = 1.0$. Each lens galaxy is simulated using two centrally aligned Sérsic profiles and a PL mass profile. Sources are simulated using either a single Sérsic profile or a superposition of between 1 and 6 elliptical (Elson, Fall & Freeman 1987, hereafter EFF) profiles,

$$I_{\rm EFF}(\xi) = I_{\rm c}(1 + r^2/r_{\rm c}^2)^{-\eta}, \quad \text{(B1)}$$

where $r_{\rm c}$ is a scale factor that relates the profile to the circular half light radius and η controls the intensity gradient of the profile. The EFF profile is used by Cornachione et al. (2018) to model the BELLS-GALLERY source galaxies, and we adopt parameter values representative of their results. We assume $\eta = 1.5$ for all simulated sources.

We simulate four baseline models of lens light, lens mass, and source light (see Tables B1 and B2). The same mass model is used to simulate lenses one and three, which forms a nearly complete Einstein ring but with either a single Sérsic source or six EFF profiles. For each lens, we create four mock images with subhaloes of mass $10^{10.5}$, $10^{10.0}$, and $10^{9.5}\,{\rm M}_\odot$ or where the subhalo is omitted. The $(x^{\rm sub},\ y^{\rm sub})$ coordinates of each subhalo are chosen to be near or on top of the lensed source's emission, to ensure they perturb the source's emission significantly enough to be detectable and thus able to test our subhalo scanning analysis.

The four images including a $10^{10.5}\,{\rm M}_\odot$ subhalo are shown in Fig. B1, where the subhalo locations are shown by a black star. Each simulated image has a resolution and S/N representative of the *HST* imaging of strong lenses we fit in this work. For $\rm Lens_1$ and $\rm Lens_2$ (which assume a single Sérsic source) we assume a pixel scale of 0.05 arcsec. For $\rm Lens_3$ and $\rm Lens_4$ (which assume EFF profiles for the source) we assume 0.04 arcsec. These pixel scales are the resolution of the SLACS and BELLS-GALLERY *HST* images, respectively. To create the images of the lens and source emission an iterative grid is used. This first evaluates each light profile (including ray-tracing if it is in the source plane) at the centre of each image pixel. It then evaluates the profiles using higher resolution subgrids within each image pixel, in increments of 11×11, 21×21, 31×31, up to 301×301. A pixel intensity is computed until it reaches a fractional accuracy of 99.9999 per cent compared to the value computed using the previous subgrid. This image has a uniform background sky added to it, is blurred with a Gaussian PSF with $\sigma = 0.05$ arcsec, has Poisson noise added, and then the input background sky subtracted.

This mock sample is idealized, in that the same lens light model (a double Sérsic) and mass model (a PL plus shear) used to simulate each lens is assumed when we fit it. The primary purpose of this exercise is to build confidence that our method does not produce false positives in this idealized setup, and determine to what masses it can accurately recover input DM subhaloes.

B2 Results

This section presents the results of fitting the 16 simulated lenses with our subhalo scanning pipeline. We perform two independent fits to every lens using a Voronoi mesh with the default 3.5 arcsec circular mask and an annular mask, where the outer and inner radii are chosen to be small whilst still containing all lensed source emission and the lens light subtraction is fixed to the maximum-likelihood lens light model inferred using a circular mask. Table B3 shows the inferred $\Delta \ln \mathcal{Z}$ values for every lens, and the inferred subhalo locations and masses for the annular mask fits, with errors quoted at 3σ confidence intervals.

We begin with the subhalo scanning results for the four simulated lenses which do not contain a DM subhalo, to verify that our analysis does not produce false positives. The 1st, 5th, 9th, and 13th rows of Table B3 show the inferred $\Delta \ln \mathcal{Z}$ values for each fit. For $\rm Lens_1$, $\rm Lens_2$, and $\rm Lens_3$ fits using either a circular or annular mask produce $\Delta \ln \mathcal{Z}^{\rm Base} < 10.0$ and therefore correctly do not favour the inclusion of a DM subhalo in the lens model. However, for $\rm Lens_4$, the subhalo scan using the 3.5 arcsec circular mask infers $\Delta \ln \mathcal{Z}^{\rm Base} = 15.25$, incorrectly favouring a DM subhalo even though one is not present in the data. The corresponding annular mask result infers $\Delta \ln \mathcal{Z}^{\rm Vor} = 2.34$, which is correctly below 10. Complex and compact sources (similar to those in BELLS-GALLERY) therefore may produce false positives when there is insufficient resolution in the source mesh to resolve it. In the main paper, fits are therefore performed to the *HST* data using source-only masks which dedicate higher resolution to the source reconstruction (annular masks are not used in the main paper due to lens light residuals requiring a more bespoke masking scheme to remove them). For the simulated lens results, we discuss hereafter only fits using annular masks.

The $\Delta \ln \mathcal{Z}$ values for the 12 other lenses which include subhaloes of mass $10^{9.5}$, $10^{10.0}$, or $10^{10.5}\,{\rm M}_\odot$ are also shown in Table B3. Fig. B2 shows their corresponding 5×5 subhalo grid searches for the Voronoi mesh with an annular mask. For all four lenses in our sample including a $10^{10.5}\,{\rm M}_\odot$ subhalo, a model including a subhalo is favoured, with $\Delta \ln \mathcal{Z}^{\rm Base}$ values of 186.58, 15.3, 638.2, and 89.54. Three $10^{10.0}\,{\rm M}_\odot$ subhaloes are also recovered with $\Delta \ln \mathcal{Z}^{\rm Base}$ values of 39.89, 7.57, 108.11, and 18.24. The $10^{9.5}\,{\rm M}_\odot$ subhaloes are recovered in $\rm Lens_1$ and $\rm Lens_3$ with $\Delta \ln \mathcal{Z}^{\rm Base}$ values of 17.67 and 33.75. Provided the detection criteria of $\Delta \ln \mathcal{Z} > 10.0$ is met, the

Table B1. The parameters of the mass models of the simulated lenses.

Lens name	$x^{\rm mass}$ (arcsec)	$y^{\rm mass}$ (arcsec)	$\epsilon_1^{\rm mass}$	$\epsilon_2^{\rm mass}$	$\theta_{\rm Ein}^{\rm mass}$ (arcsec)	$\gamma^{\rm mass}$	$\gamma_1^{\rm ext}$	$\gamma_2^{\rm ext}$	$x^{\rm sub}$ (arcsec)	$y^{\rm sub}$ (arcsec)
$\rm Lens_1$	0.0	0.0	− 0.023	0.0115	1.926	2.073	0.05	0.0	0.3	1.9
$\rm Lens_2$	0.0	0.0	0.019	0.109	1.1	1.9	− 0.007	0.006	0.5	1.34
$\rm Lens_3$	0.0	0.0	− 0.023	0.0115	1.926	2.073	0.05	0.0	0.3	1.9
$\rm Lens_4$	0.0	0.0	0.05	0.15	1.4	2.1	0.0	0.05	− 1.25	0.6

Table B2. The parameters of the source parameters of the simulated lenses. $\rm Lens_1$ and $\rm Lens_2$ correspond to Sérsic parameters, whereas $\rm Lens_3$ and $\rm Lens_4$ are Elson, Fall & Freeman parameters.

Lens name	x (arcsec)	y (arcsec)	ϵ_1	ϵ_2	I	$R/r_{\rm c}$	n
$\rm Lens_1$	0.01	0.01	− 0.05555	0.096225	0.3	0.3	2.5
$\rm Lens_2$	0.3	0.2	− 0.060356	− 0.165828	0.8	0.15	2.5
$\rm Lens_3$	0.0285	0.0404	− 0.24647	− 0.20769	11.585	0.03899	
	0.0711	0.1947	0.07803	0.00936	8.911	0.01015	
	− 0.0792	0.0760	− 0.35274	0.18159	6.3651	0.02594	
	0.0977	0.0726	− 0.23621	− 0.25923	5.5818	0.04237	
	− 0.0020	0.0020	0.51173	− 0.36744	2.254	0.02441	
	0.1131	0.0515	0.53965	0.05310	1.029	0.0336	
$\rm Lens_4$	− 0.2	0.02	0.53965	0.05310	1.029	0.0336	

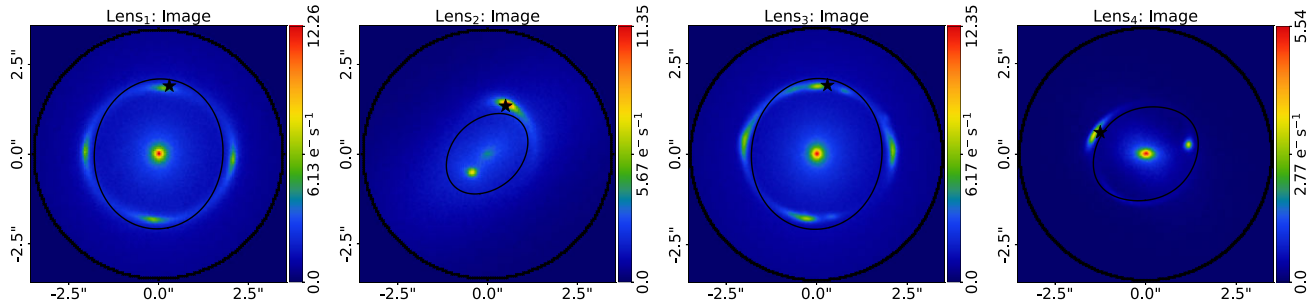

Figure B1. The simulated strong lens images we use to test PYAUTOLENS's subhalo analysis. Strong lens configurations include a quadruply imaged Einstein ring ($\rm Lens_1$ and $\rm Lens_3$) and two doubly imaged sources ($\rm Lens_2$ and $\rm Lens_4$). The source is either a single Sérsic profile ($\rm Lens_1$ and $\rm Lens_2$) or between one and six (Elson et al. 1987) light profiles ($\rm Lens_3$ and $\rm Lens_4$). Each simulated image includes a $10^{10.5}\,\rm M_\odot$ subhalo at the location marked by the black star. Images including a subhalo at these locations with masses of $10^{10.0}$ and $10^{9.5}\,\rm M_\odot$ and without a subhalo are also fitted in this work.

subhalo positions are recovered in all but one lens and masses are recovered – in all but three lenses – within the 3σ credible regions of the posteriors. For these three lenses, the masses are close to the input, but are offset due to a slightly inaccurate lens mass model (see Appendix B4).

When a subhalo is present in the data, cells away from the subhalo's true location may show smaller increases in evidence, both in the cells neighbouring the true subhalo and further away but in proximity to the lensed source's emission. For example, in the top-right panel of Fig. B2 ($\rm Lens_1$ with a $10^{10.5}\,\rm M_\odot$ DM subhalo) values of $\Delta \ln \mathcal{Z}^{\rm Base} > 150$ are seen surrounding the true subhalo (black star), but values of $\Delta \ln \mathcal{Z}^{\rm Base} > 50$ are also seen towards the bottom right and bottom left of the grid. These models infer subhalo masses above or below the true input value in order to produce a lensing signal that is similar to the signal produced by the true DM subhalo. These are not false positives, because they are due to a subhalo being truly present somewhere in the data. Models which assume a subhalo offset from a true subhalo can therefore mimic its perturbing effect by rescaling its mass. The same behaviour is discussed in He et al. (2023) and therefore must be considered when interpreting the SLACS and BELLS-GALLERY lenses. This also highlights the multimodality of the lens model parameter space and demonstrates why our grid search of `dynesty` fits removes it.

Our subhalo analysis therefore successfully detect DM subhaloes down to masses of at least $10^{9.5}\,\rm M_\odot$ for *HST*-quality data. It does not infer false positives, provided there is sufficient resolution in the source reconstruction. These conclusions are only valid for simulated data where the parametric lens light and mass models used to simulate the images are the same as those used to fit them.

B3 Justification of source analysis

Columns 8–10 of Table B3 show subhalo scanning results for fits using annular masks and the following source analysis variants: (i) switching off Voronoi natural neighbour interpolation such that each image subpixel maps to one Voronoi cell; (ii) using the Voronoi mesh equivalent of gradient regularization (see WD03; Nightingale & Dye 2015) and; (iii) doing both simultaneously. The subhalo inferences are as good as before. For all lenses not including a subhalo the different source variants correctly do not favour a subhalo, and when

Table B3. The results for fits to the simulated strong lens sample, including Bayesian evidence increases $\Delta \ln \mathcal{Z}$ of the subhalo scanning analysis where log evidence increases are computed compared to the lens model fitted without a subhalo. All mass models assume a PL plus shear and a lens light subtraction consisting of two Sérsic profiles. Bold text indiciates a log evidence increase above the subhalo detection threshold of 10.

Lens name	Subhalo mass	$\Delta \ln \mathcal{Z}^{\rm Base}$ (circular mask)	$\Delta \ln \mathcal{Z}^{\rm Base}$ (annular mask)	$x^{\rm sub}$ [arcsec]	$y^{\rm sub}$ [arcsec]	$\log_{10}[M_{200}^{\rm sub}/{\rm M}_\odot]$	$\Delta \ln \mathcal{L}^{\rm Base}$ (no interpolation)	$\Delta \ln \mathcal{L}^{\rm Base}$ (linear regularization)	$\Delta \ln \mathcal{L}^{\rm Base}$(both)	$\ln \mathcal{Z}^{\rm Base}$ (annular mask)	$\ln \mathcal{L}^{\rm Base}$ (both)	$\ln \mathcal{L}^{\rm Base}$ (linear regularization)	$\ln \mathcal{L}^{\rm Base}$ (no interpolation)
$\rm Lens_1$	No subhalo	−1.57	1.7	$0.92^{+1.84}_{-1.32}$	$1.24^{+1.42}_{-1.76}$	$9.34^{+0.69}_{-3.11}$	−0.18	−1.11	−2.1	8491.03	7782.59	7862.74	8468.02
$\rm Lens_1$	$10^{9.5}\,{\rm M}_\odot$	**12.91**	**17.67**	$1.88^{+0.65}_{-0.15}$	$0.21^{+0.18}_{-0.20}$	$9.59^{+0.27}_{-0.34}$	3.35	**28.26**	**16.75**	8565.95	7897.7	7975.78	8543.27
$\rm Lens_1$	$10^{10.0}\,{\rm M}_\odot$	**30.42**	**39.89**	$1.78^{+0.17}_{-0.13}$	$0.27^{+0.07}_{-0.06}$	$9.90^{+0.21}_{-0.28}$	**33.78**	**33.13**	**33.24**	8451.39	7788.9	7873.59	8434.49
$\rm Lens_1$	$10^{10.5}\,{\rm M}_\odot$	**181.04**	**186.58**	$1.89^{+0.11}_{-0.08}$	$0.31^{+0.05}_{-0.04}$	$10.43^{+0.10}_{-0.13}$	**119.8**	**202.16**	**177.6**	8610.81	7961.62	8038.45	8581.56
$\rm Lens_2$	No subhalo	0.76	0.45	$0.89^{+1.32}_{-2.55}$	$2.26^{+2.30}_{-2.57}$	$8.47^{+2.47}_{-2.41}$	−0.19	**13.35**	−0.22	10319.48	8659.13	8737.79	10276.96
$\rm Lens_2$	$10^{9.5}\,{\rm M}_\odot$	**12.12**	3.71	$-0.53^{+1.22}_{-1.22}$	$1.72^{+1.73}_{-2.46}$	$10.66^{+0.33}_{-4.05}$	3.56	**17.52**	1.28	10245.35	8525.47	8690.09	10199.79
$\rm Lens_2$	$10^{10.0}\,{\rm M}_\odot$	**15.6**	7.57	$1.48^{+1.16}_{-0.40}$	$0.44^{+0.24}_{-0.70}$	$9.95^{+0.48}_{-1.44}$	5.05	3.87	**12.25**	10277.55	8599.48	8731.97	10234.11
$\rm Lens_2$	$10^{10.5}\,{\rm M}_\odot$	**12.83**	**15.3**	$1.50^{+0.17}_{-0.20}$	$0.50^{+0.14}_{-0.11}$	$10.35^{+0.38}_{-0.60}$	**16.95**	**14.25**	**56.05**	10309.66	8522.58	8556.9	10278.37
$\rm Lens_3$	No subhalo	5.68	4.62	$-1.81^{+1.82}_{-2.68}$	$0.10^{+2.20}_{-1.68}$	$8.04^{+1.52}_{-2.03}$	0.06	−6.14	−1.39	13846.96	12640.44	12833.41	13817.07
$\rm Lens_3$	$10^{9.5}\,{\rm M}_\odot$	**58.99**	**33.75**	$1.95^{+0.21}_{-0.31}$	$0.41^{+0.25}_{-0.12}$	$9.43^{+0.38}_{-0.32}$	**13.51**	**37.86**	**38.01**	13895.6	12756.99	12908.08	13882.19
$\rm Lens_3$	$10^{10.0}\,{\rm M}_\odot$	**128.92**	**108.11**	$1.90^{+0.09}_{-0.09}$	$0.27^{+0.06}_{-0.05}$	$9.87^{+0.18}_{-0.13}$	**57.36**	**123.86**	**107.06**	13872.69	12697.12	12893.02	13846.19
$\rm Lens_3$	$10^{10.5}\,{\rm M}_\odot$	**431.22**	**638.2**	$1.95^{+0.07}_{-0.04}$	$0.33^{+0.04}_{-0.03}$	$10.70^{+0.09}_{-0.08}$	**274.93**	**595.63**	**531.53**	13867.75	12788.37	12918.48	13865.25
$\rm Lens_4$	No subhalo	**15.25**	2.34	$-0.16^{+1.71}_{-2.12}$	$1.17^{+2.17}_{-2.52}$	$8.09^{+2.45}_{-1.76}$	−0.08	3.93	−1.1	15447.45	14188.7	14285.39	15416.03
$\rm Lens_4$	$10^{9.5}\,{\rm M}_\odot$	**34.71**	3.61	$0.71^{+0.85}_{-1.38}$	$-1.30^{+1.54}_{-1.58}$	$9.05^{+1.52}_{-2.56}$	0.96	**32.49**	**12.93**	15370.66	14119.52	14191.89	15343.7
$\rm Lens_4$	$10^{10.0}\,{\rm M}_\odot$	**53.36**	**18.24**	$0.70^{+0.05}_{-0.18}$	$-1.28^{+0.12}_{-0.10}$	$9.79^{+0.29}_{-0.32}$	**10.8**	**10.9**	**29.02**	15394.6	14146.35	14201.78	15372.61
$\rm Lens_4$	$10^{10.5}\,{\rm M}_\odot$	**186.26**	**89.54**	$0.63^{+0.05}_{-0.04}$	$-1.43^{+0.11}_{-0.16}$	$10.38^{+0.15}_{-0.24}$	**70.11**	**105.94**	**111.36**	15195.02	14003.25	14080.38	15216.3

Notes. Columns 3 and 4 show results using the baseline Voronoi source analysis, which includes natural neighbour interpolation and brightness-based regularization. Column 3 shows $\Delta \ln \mathcal{Z}^{\rm Base}$ using a 3.5 arcsec circular mask and column 4 for an annular mask. Columns 5–7 show the inferred subhalo location $x^{\rm sub}$, $y^{\rm sub}$, and mass $\log_{10}[M_{200}^{\rm sub}/{\rm M}_\odot]$ for the fit using an annular mask, where errors are quoted at 3σ credible regions. The true input subhalo coordinates ($x^{\rm sub}$, $y^{\rm sub}$) for each lens are:$\rm Lens_1 = (0.3\,arcsec,\ 1.9\,arcsec)$, $\rm Lens_2 = (0.5\,arcsec,\ 1.34\,arcsec)$, $\rm Lens_3 = (0.3\,arcsec,\ 1.9\,arcsec)$, and $\rm Lens_4 = (-1.25\,arcsec,\ 0.6\,arcsec)$. Columns 8–10 show results for three source analysis variants (all using annular masks), which respectively: (i) switch off Voronoi natural neighbour interpolation such that every image subpixel maps to only one source pixel; (ii) use linear regularization (see Warren & Dye 2003; Nightingale & Dye 2015) instead of brightness-based adaptive regularization and; and (iii) make both changes simultaneously. The final four columns show the overall Bayesian evidence values, $\ln \mathcal{Z}$, inferred for all four source analysis variants in the final model fit which includes a DM subhalo. These can be compared to choose the optimal source analysis.

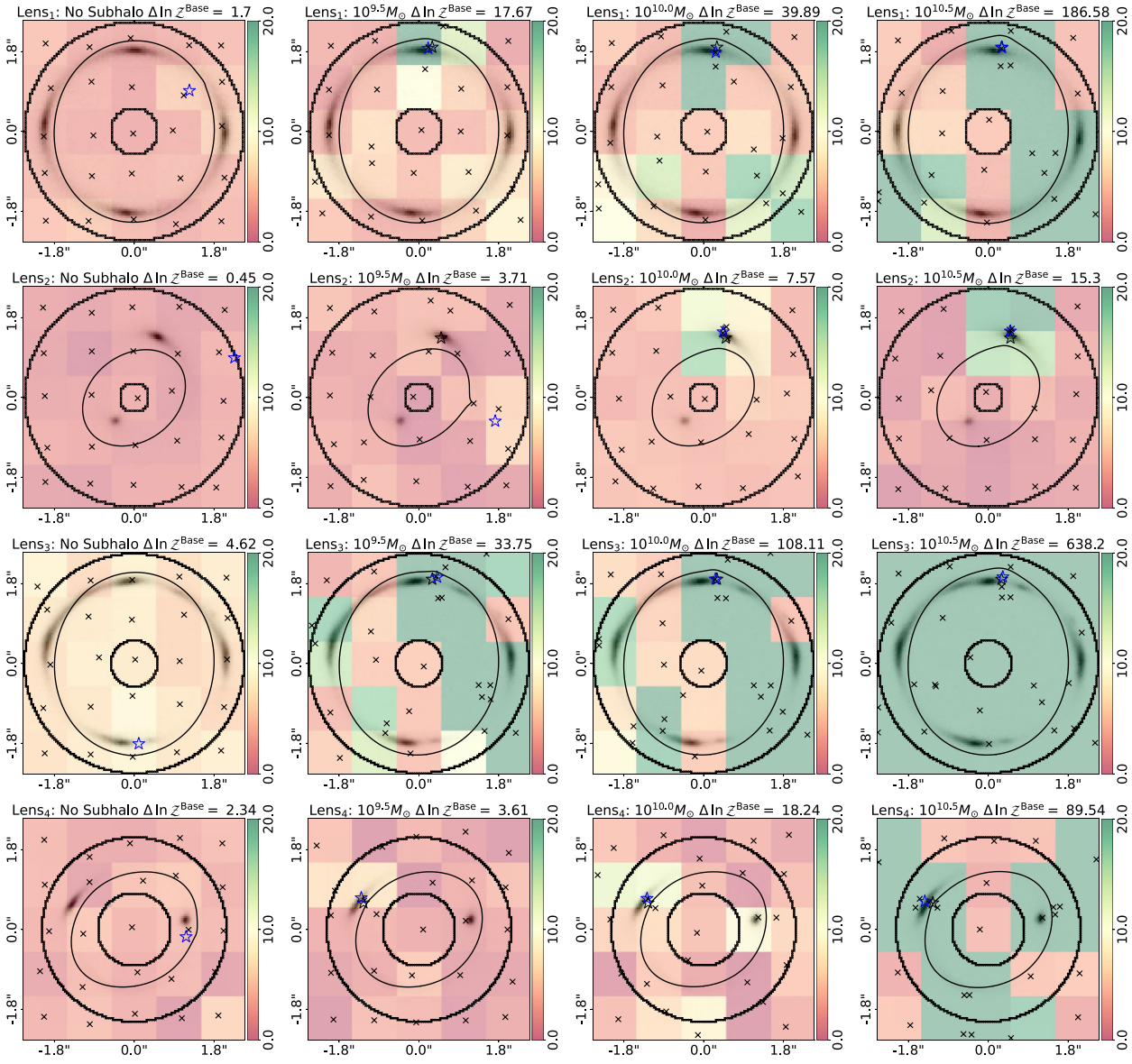

Figure B2. The Bayesian evidence increases $\Delta \ln \mathcal{Z}^{\rm Base}$ inferred by the subhalo scan for every simulated lens. Fits use a Voronoi mesh source reconstruction, annular masks and a PL plus shear model with and without a subhalo. Each panel shows a 5 × 5 grid of `dynesty` non-linear searches where the grid of overlaid values shows $\Delta \ln \mathcal{Z}^{\rm Base}$ values. The input subhalo mass increases from left to right and different lenses are shown across the rows. The (y, x) coordinates of each subhalo are confined to the 2D grid cell via uniform priors and the inferred values are shown by crosses. The true subhalo location is marked with a star. The star shows the DM subhalo's maximum a posteriori inferred location for this fit. The colour bar ranges between 0 and 20 so that candidate DM subhaloes ($\Delta \ln \mathcal{Z}^{\rm Base} > 10$) are coloured distinctly from non-candidates.

a subhalo is included it is recovered in the majority of lenses. Our DM subhalo results are therefore not sensitive to the specifics of the source analysis. This is because a Bayesian evidence increase of $\Delta \ln \mathcal{Z} > 10$ corresponds to a $\gtrsim 5\sigma$ result. Changing such a large Bayesian evidence increase via the source regularization or interpolation would require a much more radical change in the priors about how smooth galaxies are.

The final four columns of Table B3 show the overall log Bayesian evidence values, $\ln \mathcal{Z}$, using the different source variants for the lens model including a DM subhalo. These can be compared in order to determine the optimal source analysis. In 15 out of 16 lenses, the highest evidence source analysis uses both natural neighbour Voronoi interpolation and adaptive luminosity-based regularization, justifying our choice to use it in the main paper. Table B3 shows that using adaptive regularization is more important than interpolation, a result that is consistent with the findings of Nightingale et al. (2018), in particular figs 6–8, and Section 5, who showed that for compact sources different regions of the source reconstruction require different levels of regularization in order to ensure a clean reconstruction, a result also discussed by Vegetti et al. (2014). Recently, Vernardos & Koopmans (2022) performed a similar comparison of different source methods and argued in favour of 'observationally motivated priors' for the source regularization. Detailed comparison is beyond the scope of this work.

B4 Mass models adjust parameters to absorb subhalo perturbation

Table B4 shows the PL plus shear mass models inferred directly before the subhalo search. For all data sets without a subhalo, the inferred parameters are accurate and consistent with the input values given in Table B1. However, for certain data sets including a high-mass subhalo, offsets from the true parameter values are seen. The most extreme example is for Lens_3 with a $10^{10.5}$ $\mathrm{M}_\odot$ subhalo. A density slope of $\gamma^{\mathrm{mass}} = 2.6520^{+0.0391}_{-0.0244}$ is inferred compared to $\gamma^{\mathrm{mass}} = 2.0616^{+0.0767}_{-0.0736}$ for data without a subhalo (the true value is $\gamma^{\mathrm{mass}} = 2.073$). The magnitude of the offsets vary across the other data sets and across different mass model parameters (but not the external shear parameters). Furthermore, the offsets decrease as the input subhalo mass is reduced. This is evidence that the PL mass model is adjusting its parameters to 'absorb' the perturbing effect of the subhalo in certain lenses, impacting our ability to detect the DM subhalo.

The normalized residuals of the PL model fits to the simulated data sets using a Voronoi mesh and annular mask are shown in Fig. B3. The four simulated lenses run from top to bottom, with the input subhalo mass decreasing from left to right (the right most panel shows data without a subhalo). The presence of a $10^{10.5}$ $\mathrm{M}_\odot$ subhalo creates residuals in the majority of fits. These show characteristic features of subhalo residuals that are localized primarily around a single image of the lensed source near the subhalo's true location, marked on Fig. B3 as a black star (Vegetti & Koopmans 2009; Vegetti et al. 2010). There are lenses where a $10^{10.5}$ $\mathrm{M}_\odot$ subhalo does not produce visible residuals, which overlap with the lenses whose PL model is offset from the true input model, reaffirming the notion that changes to the mass model may absorb the subhalo signal. For lenses where no subhalo is included (right columns), the residuals are consistent with Gaussian noise. A lack of visible residuals does not necessarily mean that a subhalo is undetectable, because the source reconstruction has the flexibility to adapt its reconstruction to account for the subhalo perturbation. One may still ultimately infer an evidence increase in the subhalo scanning analysis because the inclusion of the subhalo improves the likelihood via the regularization terms (see Suyu et al. 2006).

The largest offsets of mass model parameters for data with high-mass subhaloes are seen in Lens_3 and Lens_4, which are the simulated lenses with complex and compact sources (e.g. BELLS-GALLERY like). For more compact sources the mass model therefore appears more able to absorb the subhalo signal. This is consistent with the results of Ritondale et al. (2019b) who performed sensitivity mapping of the BELLS-GALLERY lenses and noted reduced sensitivity due to weaker constraints on the mass model parameters for more compact sources.

The centre of PL mass models which absorb high-mass DM subhaloes are also offset from their true values of (0.0 arcsec, 0.0 arcsec). For example, for Lens_3 with a $10^{10.5}$ $\mathrm{M}_\odot$ subhalo the inferred centre is $(x^{\mathrm{mass}}, y^{\mathrm{mass}}) = (0.005\,\mathrm{arcsec}, 0.003\,\mathrm{arcsec})$ and for Lens_4 it is $(x^{\mathrm{mass}}, y^{\mathrm{mass}}) = (0.002\,\mathrm{arcsec}, 0.012\,\mathrm{arcsec})$. Both these centres are offset from (0.0 arcsec, 0.0 arcsec) at 3σ confidence. The decomposed mass models fitted in this work tie the 2D stellar mass distribution to the emission of the lens galaxy's light, and therefore put strong constraints on the stellar mass profile centre (as well as the ellipticity components). This may reduce a decomposed mass model's ability to absorb a DM subhalo signal.

Table B4. The median PDF parameter estimates with 3σ confidence intervals for the PL + shear model fits to each simulated lens data set. Fits use a Voronoi mesh and annular mask and are performed directly before the subhalo detection grid search.

Lens name	Subhalo mass	$\epsilon_1^{\rm mass}$	$\epsilon_2^{\rm mass}$	$\theta_{\rm Ein}^{\rm mass}$ (arcsec)	$\gamma_1^{\rm ext}$	$\gamma_2^{\rm ext}$	$y^{\rm mass}$ (arcsec)	$x^{\rm mass}$ (arcsec)	$\gamma^{\rm mass}$
$\rm Lens_1$	No subhalo	$0.0106^{+0.0033}_{-0.0029}$	$-0.0159^{+0.0054}_{-0.0051}$	$1.9244^{+0.0031}_{-0.0021}$	$-0.0005^{+0.0015}_{-0.0022}$	$0.0524^{+0.0080}_{-0.0040}$	$-0.0000^{+0.0013}_{-0.0015}$	$0.0005^{+0.0015}_{-0.0013}$	$2.0725^{+0.1129}_{-0.0636}$
$\rm Lens_1$	$10^{9.5}\,\rm M_\odot$	$0.0143^{+0.0036}_{-0.0028}$	$-0.0250^{+0.0049}_{-0.0047}$	$1.9273^{+0.0044}_{-0.0040}$	$0.0013^{+0.0019}_{-0.0017}$	$0.0485^{+0.0066}_{-0.0066}$	$0.0005^{+0.0016}_{-0.0017}$	$0.0003^{+0.0010}_{-0.0011}$	$2.0509^{+0.0997}_{-0.0937}$
$\rm Lens_1$	$10^{10.0}\,\rm M_\odot$	$0.0132^{+0.0038}_{-0.0029}$	$-0.0245^{+0.0046}_{-0.0049}$	$1.9276^{+0.0046}_{-0.0040}$	$0.0010^{+0.0022}_{-0.0019}$	$0.0467^{+0.0066}_{-0.0055}$	$0.0020^{+0.0017}_{-0.0014}$	$0.0010^{+0.0012}_{-0.0012}$	$2.0180^{+0.0972}_{-0.0871}$
$\rm Lens_1$	$10^{10.5}\,\rm M_\odot$	$0.0192^{+0.0038}_{-0.0036}$	$-0.0336^{+0.0043}_{-0.0049}$	$1.9414^{+0.0042}_{-0.0056}$	$0.0024^{+0.0021}_{-0.0023}$	$0.0507^{+0.0060}_{-0.0067}$	$0.0055^{+0.0015}_{-0.0012}$	$0.0015^{+0.0010}_{-0.0012}$	$2.0913^{+0.0792}_{-0.0963}$
$\rm Lens_2$	No subhalo	$0.1179^{+0.0257}_{-0.0268}$	$0.0309^{+0.0204}_{-0.0217}$	$1.1002^{+0.0059}_{-0.0078}$	$0.0118^{+0.0184}_{-0.0193}$	$0.0003^{+0.0136}_{-0.0154}$	$-0.0089^{+0.0187}_{-0.0184}$	$-0.0089^{+0.0130}_{-0.0161}$	$1.9036^{+0.0404}_{-0.0467}$
$\rm Lens_2$	$10^{9.5}\,\rm M_\odot$	$0.1387^{+0.0327}_{-0.0211}$	$0.0202^{+0.0181}_{-0.0176}$	$1.1093^{+0.0047}_{-0.0052}$	$0.0144^{+0.0225}_{-0.0147}$	$-0.0067^{+0.0105}_{-0.0136}$	$-0.0054^{+0.0169}_{-0.0181}$	$-0.0054^{+0.0093}_{-0.0124}$	$1.9498^{+0.0423}_{-0.0382}$
$\rm Lens_2$	$10^{10.0}\,\rm M_\odot$	$0.1848^{+0.0372}_{-0.0316}$	$0.0150^{+0.0218}_{-0.0180}$	$1.1182^{+0.0089}_{-0.0082}$	$0.0388^{+0.0260}_{-0.0211}$	$-0.0055^{+0.0140}_{-0.0138}$	$0.0007^{+0.0166}_{-0.0194}$	$-0.0103^{+0.0146}_{-0.0165}$	$1.9904^{+0.0590}_{-0.0429}$
$\rm Lens_2$	$10^{10.5}\,\rm M_\odot$	$0.1643^{+0.0317}_{-0.0258}$	$-0.0019^{+0.0170}_{-0.0203}$	$1.1402^{+0.0065}_{-0.0059}$	$0.0098^{+0.0199}_{-0.0169}$	$-0.0070^{+0.0109}_{-0.0129}$	$0.0204^{+0.0130}_{-0.0141}$	$-0.0087^{+0.0112}_{-0.0116}$	$2.0662^{+0.0445}_{-0.0400}$
$\rm Lens_3$	No subhalo	$0.0109^{+0.0022}_{-0.0021}$	$-0.0227^{+0.0030}_{-0.0030}$	$1.9251^{+0.0028}_{-0.0027}$	$-0.0002^{+0.0013}_{-0.0012}$	$0.0494^{+0.0045}_{-0.0043}$	$-0.0012^{+0.0013}_{-0.0010}$	$0.0000^{+0.0009}_{-0.0010}$	$2.0616^{+0.0767}_{-0.0736}$
$\rm Lens_3$	$10^{9.5}\,\rm M_\odot$	$0.0145^{+0.0018}_{-0.0021}$	$-0.0253^{+0.0030}_{-0.0022}$	$1.9278^{+0.0032}_{-0.0035}$	$0.0015^{+0.0014}_{-0.0012}$	$0.0479^{+0.0037}_{-0.0052}$	$0.0010^{+0.0009}_{-0.0009}$	$0.0007^{+0.0010}_{-0.0009}$	$2.0431^{+0.0642}_{-0.0795}$
$\rm Lens_3$	$10^{10.0}\,\rm M_\odot$	$0.0158^{+0.0021}_{-0.0015}$	$-0.0212^{+0.0024}_{-0.0024}$	$1.9284^{+0.0027}_{-0.0033}$	$0.0022^{+0.0013}_{-0.0010}$	$0.0492^{+0.0037}_{-0.0047}$	$0.0017^{+0.0008}_{-0.0007}$	$0.0013^{+0.0009}_{-0.0008}$	$2.0356^{+0.0597}_{-0.0749}$
$\rm Lens_3$	$10^{10.5}\,\rm M_\odot$	$0.0264^{+0.0189}_{-0.0016}$	$-0.0380^{+0.0038}_{-0.0057}$	$1.9685^{+0.0110}_{-0.0026}$	$-0.0051^{+0.0052}_{-0.0005}$	$0.0882^{+0.0029}_{-0.0007}$	$0.0059^{+0.0024}_{-0.0004}$	$0.0031^{+0.0006}_{-0.0005}$	$2.6520^{+0.0391}_{-0.0244}$
$\rm Lens_4$	No subhalo	$0.1640^{+0.0167}_{-0.0132}$	$0.0486^{+0.0095}_{-0.0098}$	$1.4134^{+0.0224}_{-0.0195}$	$0.0523^{+0.0070}_{-0.0105}$	$-0.0037^{+0.0077}_{-0.0082}$	$0.0001^{+0.0061}_{-0.0063}$	$0.0019^{+0.0055}_{-0.0081}$	$2.1476^{+0.1228}_{-0.0913}$
$\rm Lens_4$	$10^{9.5}\,\rm M_\odot$	$0.1622^{+0.0178}_{-0.0161}$	$0.0561^{+0.0101}_{-0.0087}$	$1.4325^{+0.0181}_{-0.0197}$	$0.0415^{+0.0078}_{-0.0085}$	$-0.0074^{+0.0057}_{-0.0066}$	$0.0042^{+0.0046}_{-0.0050}$	$0.0017^{+0.0081}_{-0.0042}$	$2.2550^{+0.0868}_{-0.1007}$
$\rm Lens_4$	$10^{10.0}\,\rm M_\odot$	$0.1937^{+0.0291}_{-0.0139}$	$0.0541^{+0.0112}_{-0.0118}$	$1.4713^{+0.0309}_{-0.0196}$	$0.0413^{+0.0060}_{-0.0054}$	$-0.0181^{+0.0064}_{-0.0078}$	$0.0084^{+0.0053}_{-0.0041}$	$0.0018^{+0.0063}_{-0.0041}$	$2.3810^{+0.0796}_{-0.0822}$
$\rm Lens_4$	$10^{10.5}\,\rm M_\odot$	$0.2317^{+0.0251}_{-0.0270}$	$0.0733^{+0.0152}_{-0.0129}$	$1.5363^{+0.0339}_{-0.0295}$	$0.0343^{+0.0059}_{-0.0054}$	$-0.0286^{+0.0033}_{-0.0046}$	$0.0119^{+0.0040}_{-0.0041}$	$0.0015^{+0.0042}_{-0.0042}$	$2.5390^{+0.0642}_{-0.0622}$

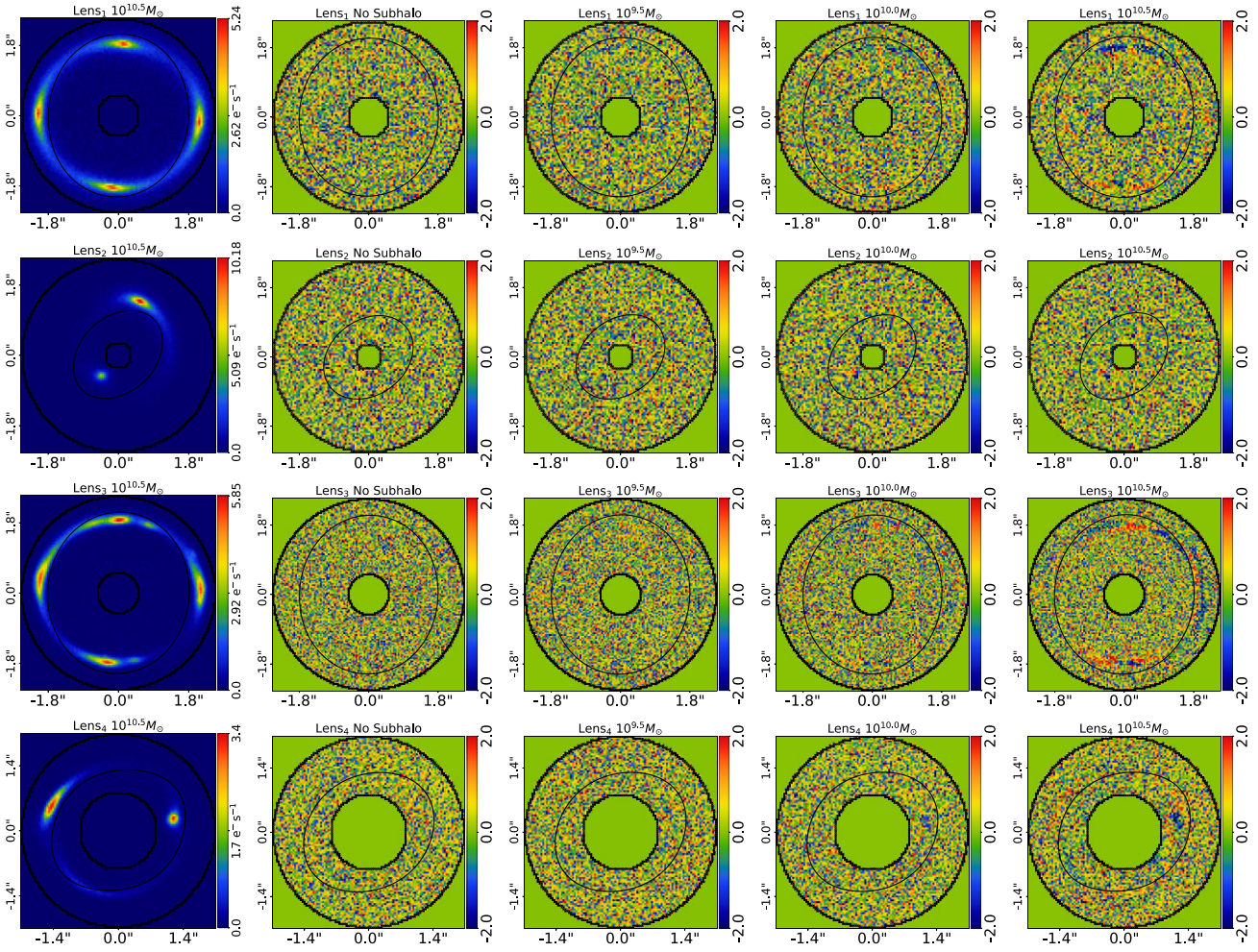

Figure B3. The lens subtracted images (left panel) and normalized residuals (data minus model divided by noise) of a PL plus shear model fit without a subhalo to each simulated data set. The lens subtracted images are for each data set with a $10^{10.5}$ $M_\odot$ subhalo. Panels to the right show the residuals for data sets where the input subhalo mass increases from left to right and different lenses are shown across the rows. Fits are shown for a Voronoi mesh source reconstruction and annular masks. The true subhalo location is marked with a black star. For certain lenses and source models, the PL plus shear model leaves residuals in the vicinity of the subhalo.

This paper has been typeset from a TEX/LATEX file prepared by the author.